Activity modulation in anaerobic ribonucleotide reductases: nucleotide binding to the ATP-cone mediates long-range order-disorder transitions in the active site

Ornella Bimaï[1], Ipsita Banerjee[2¶], Inna Rozman Grinberg[1], Ping Huang[3], Daniel Lundin[1], Britt-Marie Sjöberg[1] & Derek T. Logan*[2]

[1]Department of Biochemistry and Biophysics, Stockholm University, SE-10691 Stockholm [2]Section for Biochemistry and Structural Biology, Centre for Molecular Protein Science, Dept. of Chemistry, Lund University, SE-22100 Lund, [3]Department of Chemistry - Ångström Laboratory, Uppsala University, SE-75120 Uppsala, Sweden

¶deceased
*corresponding author

Abstract

A small, nucleotide-binding domain, the ATP-cone, is found at the N-terminus of most ribonucleotide reductase (RNR) catalytic subunits. By binding ATP or dATP it regulates the enzyme activity of all classes of RNR. Functional and structural work on aerobic RNRs has revealed a plethora of ways in which dATP inhibits activity by inducing oligomerization and preventing a productive radical transfer from one subunit to the active site in the other. Anaerobic RNRs, on the other hand, store a stable glycyl radical next to the active site and the basis for their dATP-dependent inhibition is completely unknown. We present biochemical, biophysical and structural information on the effects of ATP and dATP binding to the anaerobic RNR from *Prevotella copri*. The enzyme exists in a dimer-tetramer equilibrium biased towards dimers when two ATP molecules are bound and tetramers when two dATP molecules are bound. In the presence of ATP, *P. copri* NrdD is active and has a fully ordered glycyl radical domain (GRD) in one monomer of the dimer. Binding of dATP to the ATP-cone results in loss of activity and disordering of the GRD. The glycyl radical is formed even in the dATP-bound form, but the substrate does not bind, suggesting that dATP inhibition in anaerobic RNRs acts by disordering of the GRD more than 30 Å away from the dATP molecule, thereby preventing both substrate binding and radical mobilisation. The structures implicate a complex network of activity regulation involving the GRD, the allosteric substrate specificity site and a conserved but previously unseen flap over the active site.

Introduction

Ribonucleotide reductases (RNRs) are a family of enzymes with sophisticated radical chemistries and allosteric regulation. RNRs produce all four deoxyribonucleotides and are the only enzymes providing de novo building blocks for DNA replication and repair in all

free-living organisms. Virtually all RNRs possess an allosteric site regulating substrate specificity (the s-site), a crucial aspect of RNR that ultimately provides a balanced supply of dNTPs (Mathews, 2016, 2018). A second allosteric site (the a-site) is located in an N-terminal domain called the ATP-cone (Aravind *et al*, 2000), found in the majority of RNRs (Jonna *et al*, 2015). Whereas the s-site binds all deoxyribonucleoside triphosphates (dNTPs) and usually ATP, the a-site in the ATP-cone can only bind ATP and dATP. Binding of ATP activates RNR, and binding of dATP inhibits it (Hofer *et al*, 2012; Martínez-Carranza *et al*, 2020).

The RNR family consists of three evolutionarily related classes (I to III) with a common radical-based reaction mechanism but differing in the mode of radical generation and in quaternary structure (Högbom *et al*, 2020; Lundin *et al*, 2015). Class I, strictly aerobic RNRs, are heterotetramers consisting of two α subunits (NrdA) with binding sites for substrates and allosteric nucleotides and two β subunits (NrdB) harbouring a stable radical. Class II RNRs are either dimers or monomers with an α subunit (NrdJ) that, in addition to binding sites for substrate and allosteric nucleotides, also harbours the radical initiator cofactor adenosylcobalamin. Class III RNRs, which only function anaerobically, are dimers of an α subunit (NrdD) with a stable radical close to the active site, and binding sites for allosteric nucleotides. The radical is introduced via encounter with a specific radical-SAM enzyme called NrdG, and once activated NrdD can perform multiple turnovers in the absence of NrdG (Backman *et al*, 2017; Torrents *et al*, 2001).

The dATP-dependent inhibition has been biochemically characterised in representatives of all three RNR classes, but only structurally studied in class I. A common denominator of all inhibited class I RNRs is oligomerization, leading to disturbed radical transfer between the α and β subunits. Hitherto four different inhibitory oligomerization mechanisms have been identified: heterooctameric $\alpha_4\beta_4$ complexes in *Escherichia coli*, *Clostridium botulinum* and *Neisseria gonorrhoeae* (Ando *et al,* 2011; Martínez-Carranza *et al,* 2020; Wei *et al,* 2014), an α_4 complex in *Pseudomonas aeruginosa* (Johansson *et al,* 2016), α_6 complexes in the eukaryotes *Homo sapiens, Saccharomyces cerevisiae* and *Dictyostelium discoideum* (Ando *et al,* 2016; Brignole *et al,* 2018; Crona *et al,* 2013; Fairman *et al,* 2011), and a β_4 complex in the bacterium *Leeuwenhoekiella blandensis* (Rozman Grinberg *et al*, 2018a). All these class I oligomers involve protein-protein interactions mediated by the ATP-cone domain.

The ATP-cone is in essence restricted to RNRs and the RNR-specific repressor NrdR (Rozman Grinberg *et al*, 2022). Among RNRs it is found in about 80% of class III enzymes and about 50% of class I enzymes, but less than 10% of class II enzymes (Jonna *et al.*, 2015). The presence and function of the ATP-cone domain distinguish anaerobic RNRs from the other members of the large glycyl radical enzyme (GRE) family that are otherwise structurally and mechanistically related (Backman *et al.*, 2017). The allosteric regulation mechanisms of class III RNRs (NrdDs) from *E. coli*, bacteriophage T4 and *Lactococcus lactis* were determined several decades ago (Andersson *et al*, 2000; Eliasson *et al*, 1994; Torrents *et al*, 2000). T4NrdD was the first class III RNR structure solved (Logan *et al*, 1999), and later, structures of *Thermotoga maritima* NrdD (TmNrdD) have been published (Aurelius *et al*, 2015; Wei *et al*, 2014). However, these two NrdDs lack an ATP-cone and the structural basis for allosteric activity regulation in the class III RNRs is still an outstanding question. Here, we present structural, biochemical and biophysical studies on

the ATP-cone-containing NrdD from the human pathogen *Prevotella copri* (PcNrdD), showing that the binding of dATP causes complete disordering of the C-terminal glycyl radical-bearing domain, as well as a flap-like loop that binds across the top of the active site in the active form. This disordering is coupled to enzymatic inactivation by inhibition of substrate binding and radical transfer. The final outcome of dATP inhibition is thus blocked radical transfer in both class I and class III RNRs, but it is achieved by completely different mechanisms, i.e. oligomerization prevents radical transfer between subunits in class I RNRs but long-range induced order-disorder transitions prevent substrate binding in class III RNRs.

Results

Allosteric activity regulation by ATP and dATP

The amino acid sequence of PcNrdD suggests that it belongs to the formate-requiring class III RNRs (Burnim *et al*, 2022b; Wei *et al.*, 2014), and initial optimization of the assay composition showed that this was the case (Figure 1 - figure supplement 1). ATP-cone mediated activation of PcNrdD enzyme activity by ATP or inhibition by dATP was tested with two different substrates. With GTP as substrate the s-site was filled with dTTP as effector, and in absence of any a-site effector the basal level of GTP reduction was approximately 25 nmol/min•mg. An increasing concentration of ATP stimulated activity to a V_{max} of 470 nmol/min•mg, with an apparent K_L of 0.78 mM (Fig. 1a). On the other hand, an increasing concentration of dATP resulted in an abrupt inhibition of enzyme activity with a K_i of 26 μM (Fig. 1b). Hence, the K_i value for dATP inhibition via the ATP-cone is 30-fold lower compared to the K_L value for ATP activation via the ATP-cone.

The activation/inhibition experiments were also carried out with CTP as substrate. Specificity effectors for CTP reduction are ATP or dATP, so in these experiments both the s- and a-sites were conceivably filled with ATP or dATP, respectively. The basal level of CTP reduction in the absence of effector nucleotide was approximately 50 nmol/min•mg. An increasing concentration of ATP again stimulates enzyme activity to a V_{max} of 273 nmol/min•mg with an apparent K_L of 0.53 mM (Fig. 1c). Addition of dATP initially results in a stimulation of enzyme activity, conceivably when the s-site is filled with dATP, after which competing inhibition appears when dATP also binds to the ATP-cone (Fig. 1d). All in all, these results suggest that the ATP-cone in PcNrdD responds similarly to inhibition by dATP as has been observed before for several class I RNRs.

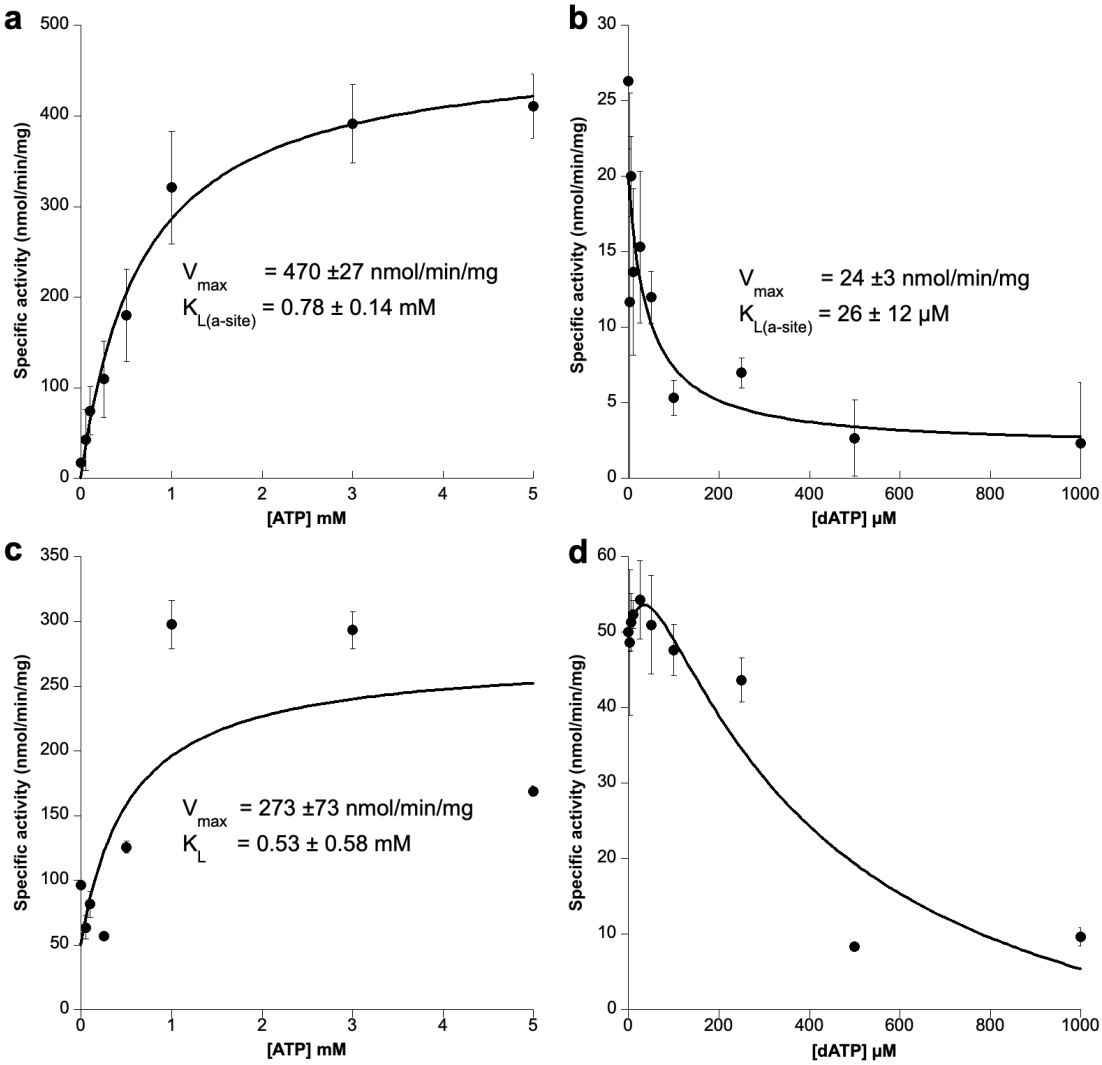

Figure 1. Activity assays of *Prevotella copri* NrdD in the presence of ATP or dATP. A 2.5-fold excess of holoNrdG over apoNrdD was used to study the allosteric regulation effect of ATP and dATP on the a-site. GTP reduction was monitored with up to 1 mM dTTP as effector in the s-site and titrated with ATP (a) or dATP (b) in the a-site. CTP reduction assays were titrated with ATP (c) or dATP (d), in this case acting both as s-site effectors and a-site regulators. Curve fits for calculation of K_L and K_i used equations given in Materials and Methods, for (c) and (d) assuming a start activity of 50 nmol/min/mg; curve fit in (d) used a combination of the two equations.

Binding of nucleotides to the ATP-cone

To confirm binding of ATP or dATP to the ATP-cone we used isothermal titration calorimetry (ITC) and microscale thermophoresis (MST) (Fig. 2). Substrate GTP and s-site effector dTTP were used to fill up the other nucleotide binding sites in PcNrdD. Binding of dATP occurred with a K_D of 6 µM, whereas binding of ATP was 4-fold weaker with a K_D of 26 µM (Fig. 2a-c). The number of bound dATP molecules observed with ITC was almost 2-fold higher for dATP compared to ATP, but both values were below 1. However, in cryo-EM experiments where higher nucleotide concentrations can be used, we show that the ATP-cone can bind two ATP or two dATP molecules (see below), as also expected based on its sequence. Nucleotide binding measured with MST confirmed our results for ATP (Fig. 2d) that had a K_D of 25 µM, and dATP that with this method had a K_D of 23 µM (Fig. 2e).

It is noteworthy that the K_D values for ATP and dATP do not differ by orders of magnitude, as has been found for several class I RNRs (Ando *et al*, 2016; Birgander *et al*, 2004; Ormö & Sjöberg, 1990; Rozman Grinberg *et al.*, 2018a; Rozman Grinberg *et al*, 2018b; Torrents *et al*, 2006). Collectively these two binding methods instead suggested that ATP and dATP may interact at two distinct sites in the ATP-cone for the functional readout of dATP inhibition, as has earlier been observed in the transcriptional repressor NrdR (Rozman Grinberg *et al.*, 2022). To test this hypothesis, apo-PcNrdD was incubated with ATP only, dATP only or a combination of ATP and dATP, then desalted, boiled, centrifuged and the nucleotide content of the supernatant analysed by HPLC. Figure 2 - figure supplement 1 shows that only dATP was bound when PcNrdD was incubated with a combination of ATP and dATP. This was also the case when incubations were performed in the presence of s-site effector and substrate, and also when the desalting was performed in the presence of s-site allosteric effector and substrate. In incubations with only ATP, s-site effector and substrate were needed during the entire work-up procedure for ATP to be retained by the protein. In conclusion, the binding experiments suggest that the PcNrdD ATP-cone can bind either ATP or dATP but not both simultaneously. Importantly, the results point to allosteric communication between the s-site, the active site and the a-site in the ATP-cone, as dTTP and GTP are required for any ATP to be retained. Both of these observations are consistent with the structural analyses shown below.

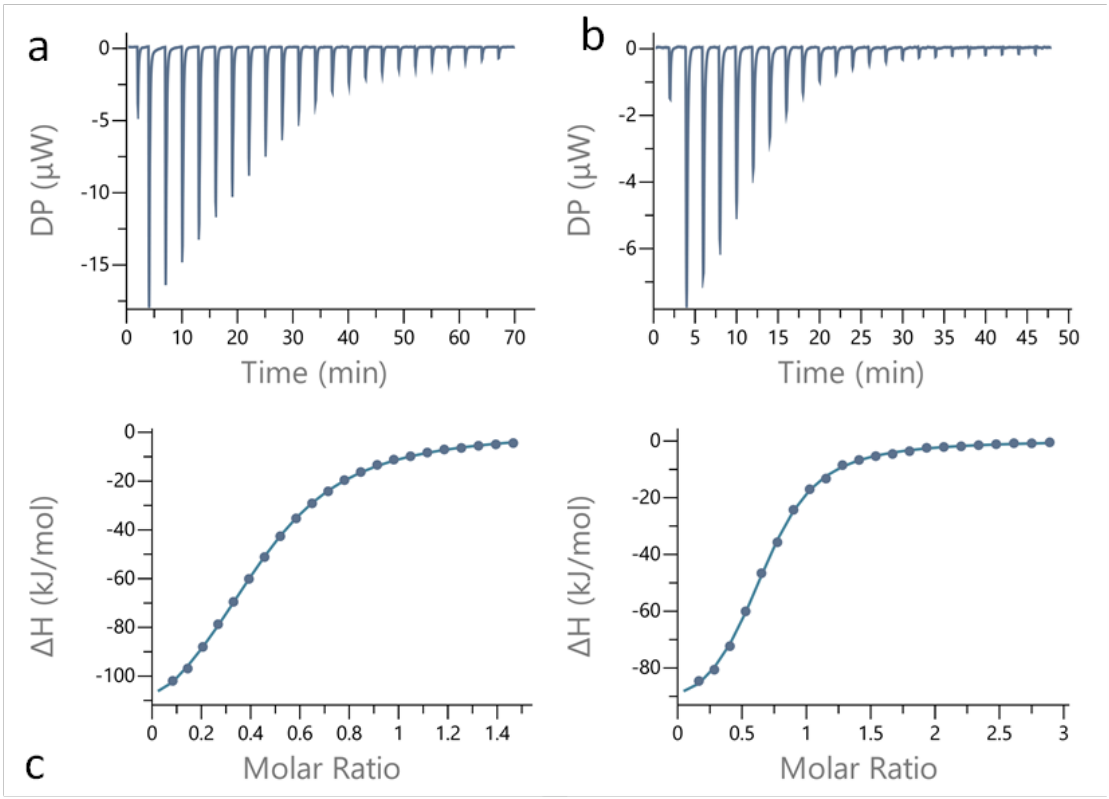

Ligand	N (sites)	K_D (µM)	ΔH (kJ/mol)	ΔG (kJ/mol)	-TΔS (kJ/mol)
ATP	0.42±0.04	26±6	-150±17	-26±0.5	125±17
dATP	0.74±0.10	5.8±3	-118±18	-30±1.1	88±19

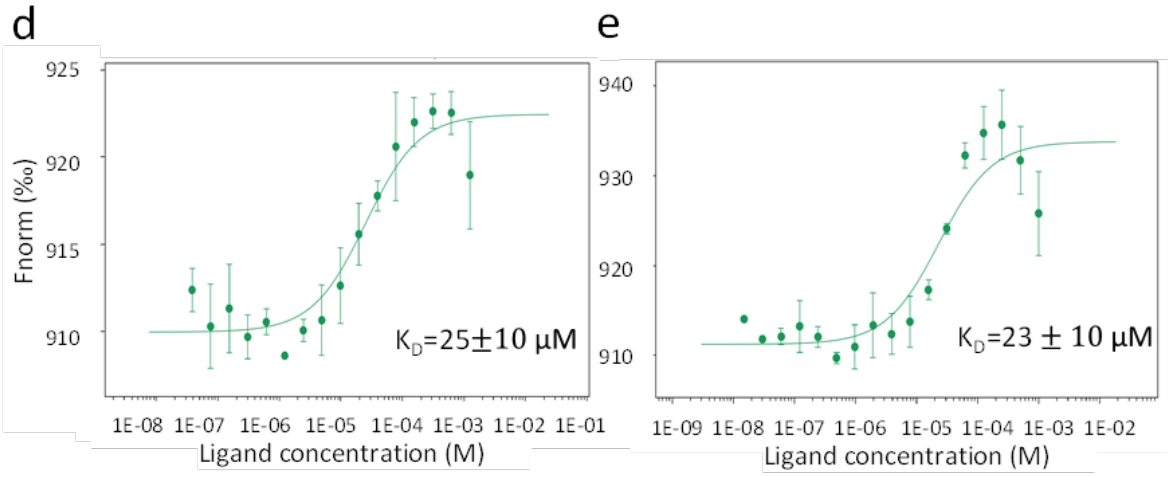

Figure 2. Binding of nucleotides to the ATP-cone. Binding assay using ITC: (a) Binding of ATP to 50 µM PcNrdD; (b) binding of dATP to 200 µM PcNrdD; (c) thermodynamic parameters of ligand binding. All titrations were performed in the presence of 1 mM GTP substrate and 1 mM s-site effector dTTP at 20 °C. Binding of nucleotides to the ATP-cone using MST: (d) Binding of ATP, (e) binding of dATP. All MST binding experiments were performed in the presence of 1 mM s-site effector dTTP and 5 mM GTP substrate at room temperature.

Modulation of the oligomeric state by ATP and dATP in the presence of allosteric effectors

Binding of dATP to the ATP-cone in all class I RNRs studied to date results in formation of higher oligomers unable to perform catalysis (Martínez-Carranza *et al.*, 2020). We therefore next asked whether a similar mechanism would be valid for dATP-mediated inhibition of a class III RNR. To elucidate the oligomeric states of PcNrdD we used gas-phase electrophoretic mobility molecular analysis (GEMMA) (Kaufman *et al*, 1996), a method based on time-of-flight mass spectrometry. It requires low protein and nucleotide concentrations as well as volatile buffers.

When loaded with ATP, PcNrdD was in a dimer-tetramer equilibrium shifted towards dimers (Fig. 3, left). Addition of the CTP substrate or the s-site effector dTTP resulted in a similar equilibrium. In contrast, the dimer-tetramer equilibrium of dATP-loaded PcNrdD was shifted towards tetramers, and this equilibrium was likewise not affected by addition of the CTP substrate (Fig. 3, right). Hence, dATP-inhibition of enzyme activity seems to work differently in PcNrdD than the clearcut and drastic change in oligomeric structure observed for class I RNRs, since both ATP-loaded and dATP-loaded forms of PcNrdD were in dimer-tetramer equilibria.

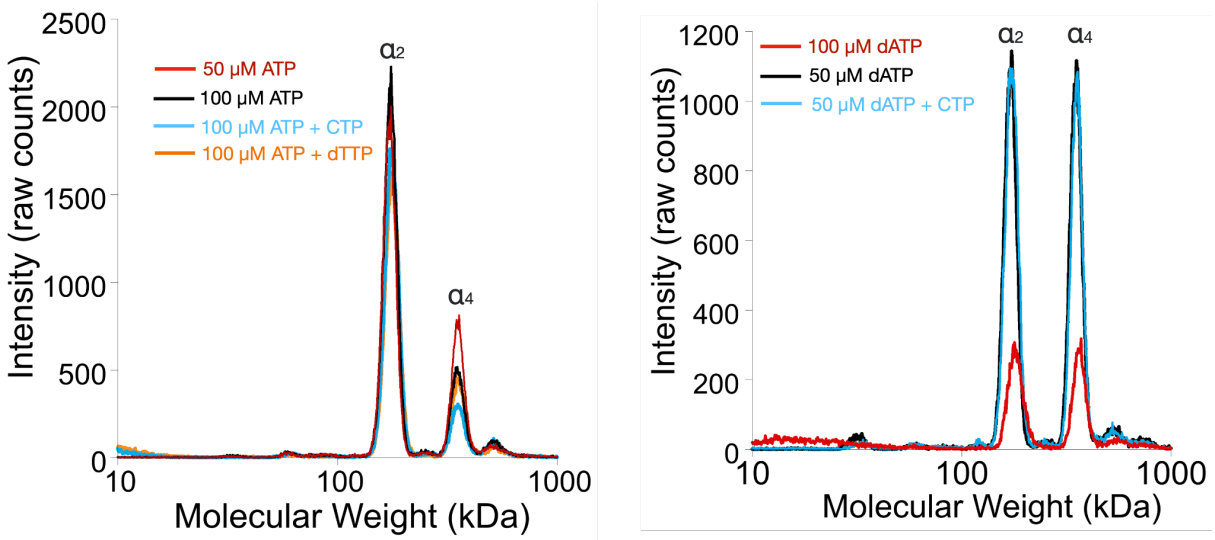

Effector(s)	Mw (kDa)	No. of monomers	Dimers vs. tetramers (%)
ATP (50 μM)	176 / 358	2.1 / 4.2	50 / 50
ATP (100 μM)	178 / 360	2.1 / 4.3	60 / 40
ATP (100 μM) + CTP	179 / 356	2.1 / 4.3	64 / 36
ATP (100 μM) + dTTP	171 / 348	2.1 / 4.2	60 / 40
dATP (50 μM)	167 / 363	2.0 / 4.3	32 / 68
dATP (100 μM)	179 / 361	2.1 / 4.3	32 / 66
dATP (50 μM) + CTP	175 / 358	2.1 / 4.2	34 / 66

Figure 3: Oligomeric states of *Prevotella copri* NrdD in the presence of nucleotides determined by GEMMA. (a) Apo-PcNrdD (2 μM) loaded with the activator ATP (50-100 μM) (black and red) in the presence of CTP (100 μM) as a substrate (cyan) or dTTP (100 μM) (orange) as the allosteric effector. (b) apo-PcNrdD (2 μM) loaded with the inhibitor dATP (50-100 μM) (black and red) in the presence of CTP (50 μM) (cyan) as the substrate.

Glycyl radical formation in presence of ATP or dATP

Next, we asked whether dATP inhibition was mediated by prevention of glycyl radical formation. Apo-PcNrdD was incubated with NrdG and *S*-adenosylmethionine in presence of ATP or dATP. Whereas reduction of substrate requires the presence of formate, the formation of a glycyl radical does not. We therefore incubated with or without formate as well as with or without substrate. Figure 4 shows that the glycyl radical was readily formed in presence of dATP both with and without the CTP substrate, and the result was similar in the absence of formate (Figure 4 - figure supplement 1). Interestingly, under all conditions the glycyl radical content was higher in the presence of dATP compared to with ATP, and it was also more stable than in absence of any effector nucleotides. In addition, the shape of the doublet EPR signal suggests that the environment of the radical was similar under all conditions studied. Collectively, these results

show that the glycyl radical is readily formed in the presence of a dATP concentration that inhibits RNR activity.

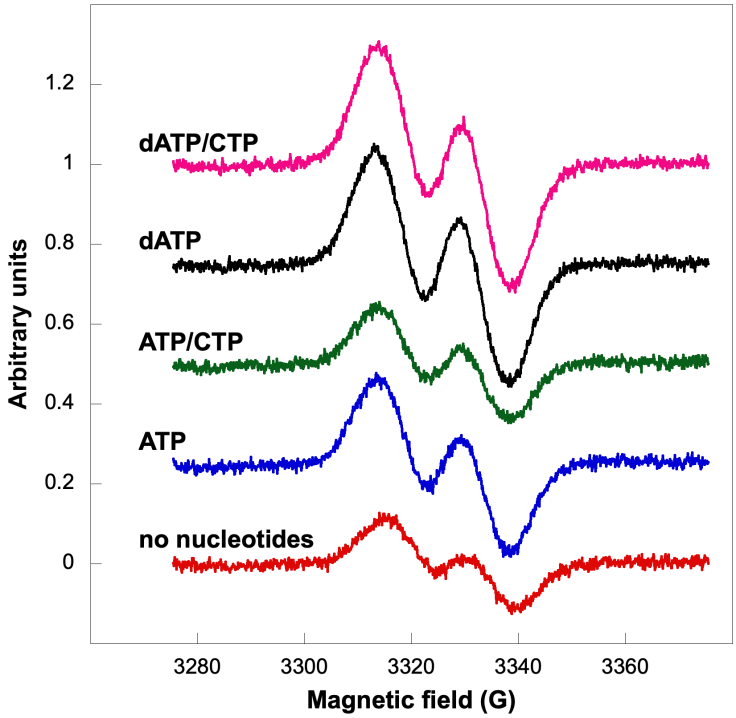

Figure 4. Glycyl radical formation after 20 min in presence of formate and ATP±CTP or dATP±CTP. Nucleotide concentrations were: 1.5 mM ATP, 1 mM dATP, and 1 mM CTP. Traces are arbitrarily moved to increase visibility and scaled to identical units (Y-axes).

Substrate binding to PcNrdD

To study substrate binding to activated and inhibited PcNrdD we used MST with labelled protein and GTP or CTP as substrate. The results were clearcut in both sets of experiments (Fig. 5). ATP-loaded PcNrdD bound GTP in the presence of s-site effector dTTP (Fig. 5a), and it bound CTP in the presence of only ATP (Fig. 5b), whereas dATP-loaded PcNrdD could bind neither GTP nor CTP under similar conditions (Fig 5c,d). These results show that the dATP-inhibition of enzyme activity in a class III RNR is mediated by inhibited binding of substrate.

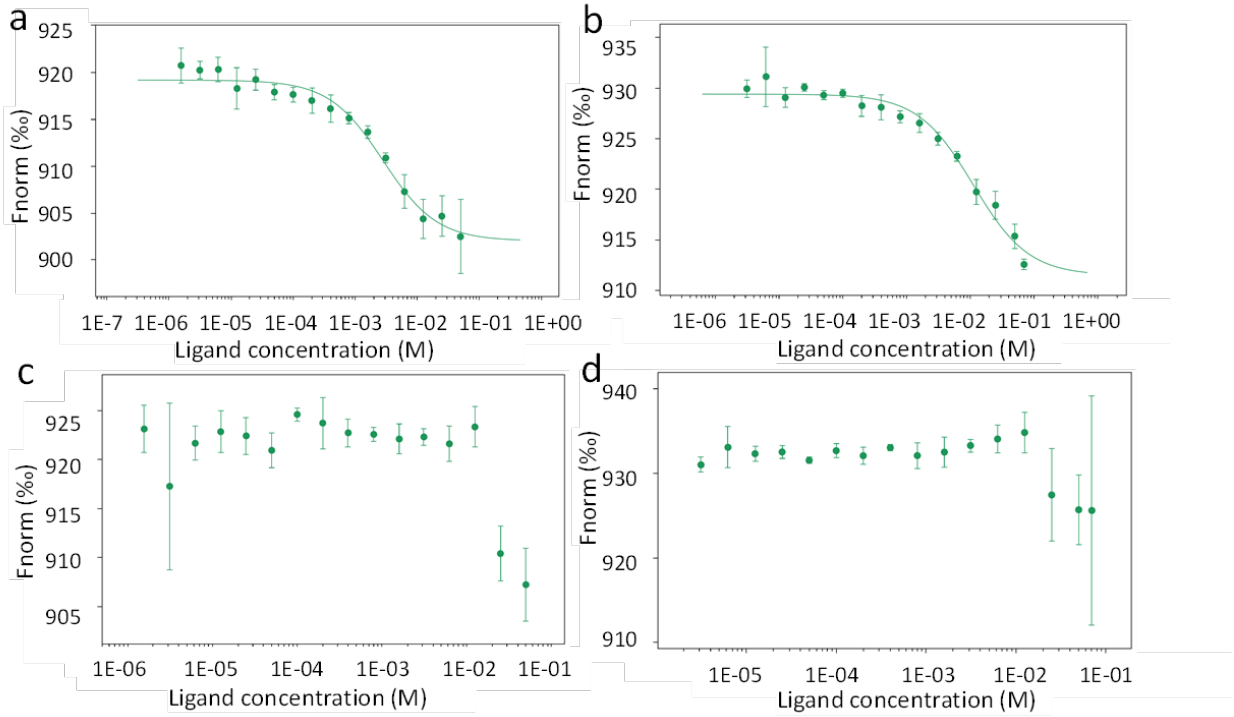

Figure 5. Binding of substrate to ATP- or dATP-loaded PcNrdD. Binding of GTP (a), and binding of CTP (b) to ATP-loaded PcNrdD. (c) Binding of GTP, and (d) binding of CTP to dATP-loaded PcNrdD. No additional nucleotides were present in CTP binding experiments, whereas binding of GTP was performed in the presence of 1 mM S-site effector dTTP. Fitted K_Ds are 2.8 ± 0.5 and 11 ± 2.4 mM for GTP and CTP binding respectively. Experiments were performed at room temperature.

Cryo-EM structure of the ATP-CTP bound PcNrdD dimer

2D classes of particles extracted from micrographs of PcNrdD incubated with effector ATP and substrate CTP indicated only dimers, with no appreciable amounts of tetramer. From a set of 570 730 particles we obtained a map from cryoSPARC at 3.0 Å. Application of deep learning local sharpening in DeepEMhancer (Sanchez-Garcia *et al*, 2021) improved the quality of the map, and we were able to build a reliable model for the great majority of the structure. As the ATP-cone density still did not permit reliable modelling, 3D classification was carried out on this particle set, enabling the identification of a subset of 291 231 particles that gave a volume at 3.2 Å with better-defined ATP-cones (Figure 6a). This map was used for refinement of the final model (Table 1; Table 1 – table supplement 1).

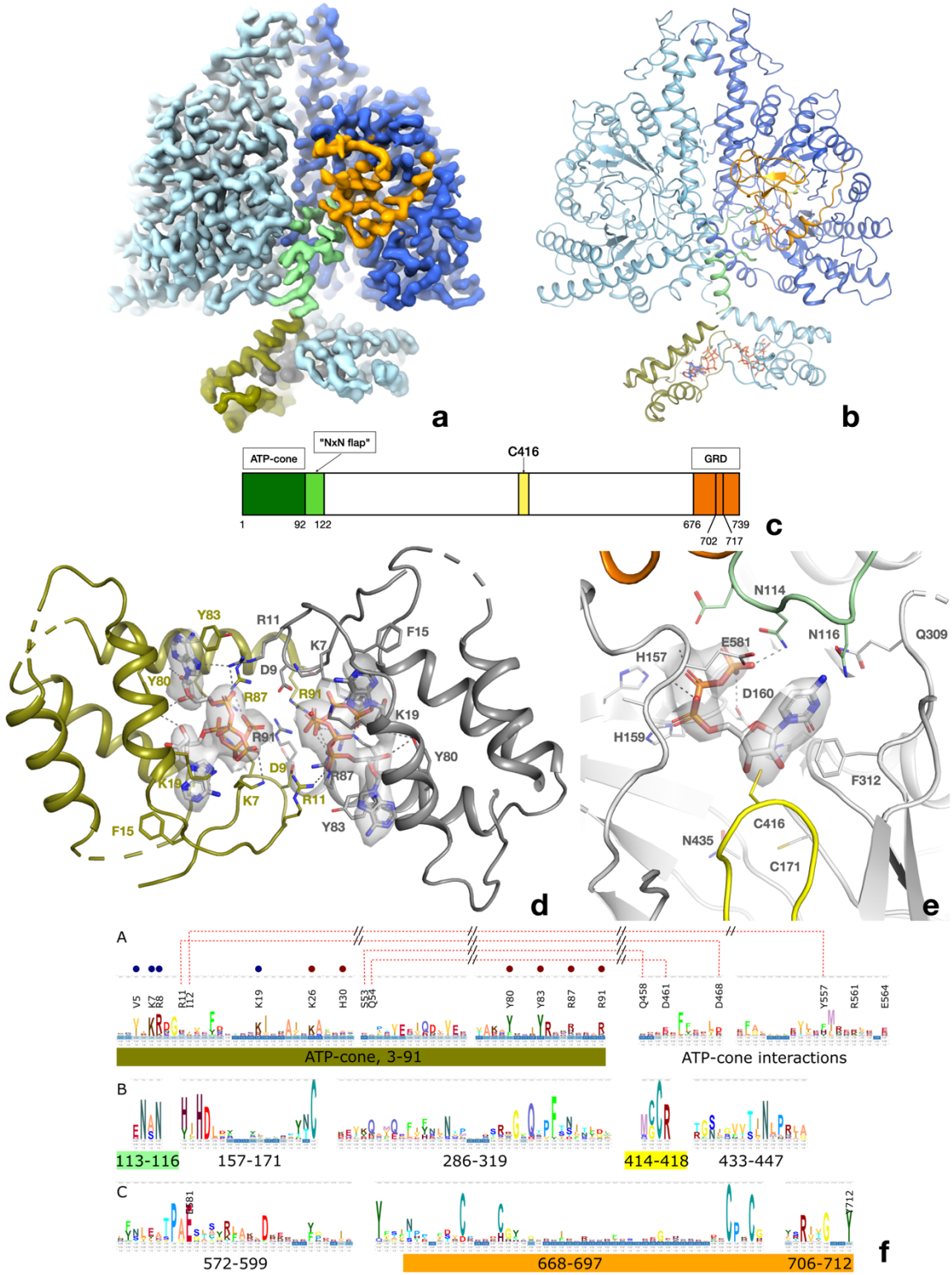

Figure 6: Structure of the PcNrdD dimer in complex with effector ATP and substrate CTP. a) cryo-EM map with C1 symmetry showing the best-ordered ATP-cones after post-processing using DeepEMhancer. For the right-hand (active) monomer, the ATP-cone (residues 1-91) and the linking helix (92-104) are coloured olive, the linker and NxN flap region pale green, the glycyl radical loop red and the C-terminal extended region orange. The loop in the middle of the α/β barrel containing the radical initiator cysteine Cys416 at its tip is yellow. b) Overview of the PcNrdD dimer with ATP and CTP. The two monomers of the dimer are coloured in different shades of grey. The ATP and CTP molecules are shown as sticks. c) Schematic of the domain organisation of PcNrdD with the same colour scheme as a) and b); d) Closeup view of the binding of four ATP molecules to the dimer of ATP-cones in PcNrdD. The view is from the

bottom of the molecule as seen in a) and b). Disordered loops are shown as dotted lines. e) Closeup view of the active site including the cryo-EM map for CTP. Residues within 4 Å of CTP are shown as sticks and polar interactions as dotted lines. f) Sequence logos of NrdD sequence motifs. A) ATP-cone plus downstream interaction partners, B) central parts of sequence and C) C-terminal parts. The numbering is from PcNrdD. Segments were selected to illustrate amino acids discussed in the text.

PcNrdD is a compact dimer (Fig. 6b). Each monomer consists of 739 residues, of which residues 1-91 constitute the ATP-cone, 92-110 a linker region, 111-121 a flap that folds over the substrate in the active site, 122-671 are the core domain with its 10-stranded α/β barrel fold typical of the RNR/glycyl radical enzyme (GRE) family, and 676-739 are the C-terminal glycyl radical domain (GRD) that contains a structural Zn site followed by the buried loop containing the radical glycine residue at position Gly711 and a C-terminal tail that extends across the surface of the protein (Figure 6b,c). The closest structural neighbours as identified by the DALI server (Holm, 2022) are the NrdDs from bacteriophage T4 (Logan *et al.*, 1999) (1H7A, 2.5 Å root mean square deviation [rmsd] in Cα positions for 535 residues, 27% sequence identity) and *T. maritima* (Aurelius *et al.*, 2015; Wei *et al.*, 2014) (4U3E, 3.0 Å rmsd for 508 residues, 16% sequence identity; Figure 6 - figure supplement 1). The linker, flap and GRD are well-ordered in one of the monomers (dark blue in Fig. 6), while in the other monomer this region is less well-ordered. We will refer to these as the “active” and “inactive” monomers respectively.

At the concentration of ATP used (1 mM), ATP is not observed to bind to the s-sites near the dimer interface. The ATP-cones containing the a-site are flexible, but the reconstruction allowed the modelling of two ATP molecules per ATP-cone and many of the most important side chains. The ATP molecules are bound similarly to the twin dATP molecules seen in the ATP-cones of *P. aeruginosa* NrdA (PaNrdA) and *L. blandensis* NrdB (LbNrdB) (Johansson *et al*, 2016; Rozman Grinberg *et al.*, 2018a), and to dATP bound to PcNrdD itself (see below). However, the ATP-cones in PcNrdD exhibit a hitherto unobserved relative orientation in which the four triphosphate groups are projected towards each other. (Fig. 6b,d). The large negative charge is compensated for by the proximity of as many as 12 Arg and Lys side chains from both monomers. The ATP-cones interact by contacts involving the “roof” of the domain (residues 1-18). Arg11 of each ATP-cone reaches over to interact with the α-phosphate group of one of the ATP molecules in the other ATP-cone, and a salt bridge is formed between Asp9 at the end of the lid and Arg91 at the end of the last helix of the other ATP-cone. Strikingly, the dimer of ATP-cones is slightly offset from the dimer axis of the core protein, such that one of them approaches the core domain of the monomer with ordered C-terminus, while the other is more distant (Fig. 6a,b). However, the closest atom of any ATP molecule is over 30 Å from the substrate CTP in the active site.

The glycyl radical site is found at Gly711, at the tip of a loop projected from the C-terminal region of the enzyme into the barrel, where it approaches the radical initiator cysteine Cys416 at the tip of a loop projected through the barrel (Fig. 6b,e). The second cysteine necessary for the radical mechanism of PcNrdD is Cys171 on the first β-strand of the barrel (Fig. 6e). Consistent with the fact that PcNrdD belongs to the group of anaerobic RNRs that use formate as overall reductant (Burnim *et al*, 2022a; Mulliez *et al*, 1995; Wei *et al.*, 2014), there is no third cysteine residue on the sixth β-strand, and its place is taken by Asn435. As usual for GREs, Gly711 is completely buried within the barrel, with no solvent-accessible surface area. The substrate CTP is bound to the active site. The base, phosphate and most of the ribose are well-defined but the density is weaker around the 5’ C-atom (Fig. 6e).

After the glycyl radical loop emerges from the α/β barrel, it traverses the top of the barrel, forming a short helix from residues 723-730 and ending in an extended tail. This conformation of the C-terminus is very similar to the one seen for TmNrdD in PDB entry 4U3E (Wei *et al.*, 2014). This tail makes few specific interactions with other residues in the core.

When compared to previously determined NrdD structures, the first common structural element is a long α-helix in the core domain stretching from Thr123 to Leu141. Between this and the ATP-cone are a linker (91-110), followed by a "flap" over the top of the active site (111-122), which passes the substrate in the active site. Two residues from the flap make H-bonds to CTP: Asn114 to the γ-phosphate group and Asn116 to the amino group of the cytosine base. We call this region the "NxN flap", as the NxN motif (114-116) is one of the most highly conserved sequence motifs in the NrdD family (Fig. 6f). This is the first time such interactions have been observed in an NrdD, as the flap corresponds to a disordered segment of 17 residues in the structures of TmNrdD and T4NrdD. However, an AlphaFold2 (Jumper *et al*, 2021) model of TmNrdD (entry Q9WYL) suggests that this linker potentially has the same conformation in TmNrdD and possibly all other NrdDs, whether or not they have an ATP-cone. As seen previously in TmNrdD, the triphosphate moiety is recognised through the conserved HxHD motif (157-160), H-bonds to the main chain atoms of a loop (577-581) following the third-last strand of the α/β barrel and the dipole of the following helix (Fig. 6f).

Significantly, the NxN flap forms the nexus of a network of interactions (Fig. 7) between the substrate, the linker to the ATP-cone, the C-terminal GRD, and "loop 2" (residues 304-311) that is responsible for communicating the substrate specificity signal from the s-site at the dimer interface to the active site (Aurelius *et al.*, 2015; Larsson *et al*, 2001; Logan *et al.*, 1999). Important interactions linking the NxN flap to the C-terminus include H-bonds from Tyr712, which immediately follows the radical Gly711, to Glu581, which bridges to both the substrate and Ala115 in the flap, as well as from Arg719 in the GRD to the main chain carbonyl groups of Asn114 and Met117 in the flap. Tyr712 is highly conserved in the NrdD family (Fig. 6f and 7). This nexus is crucial for allosteric activity regulation, as will be discussed later.

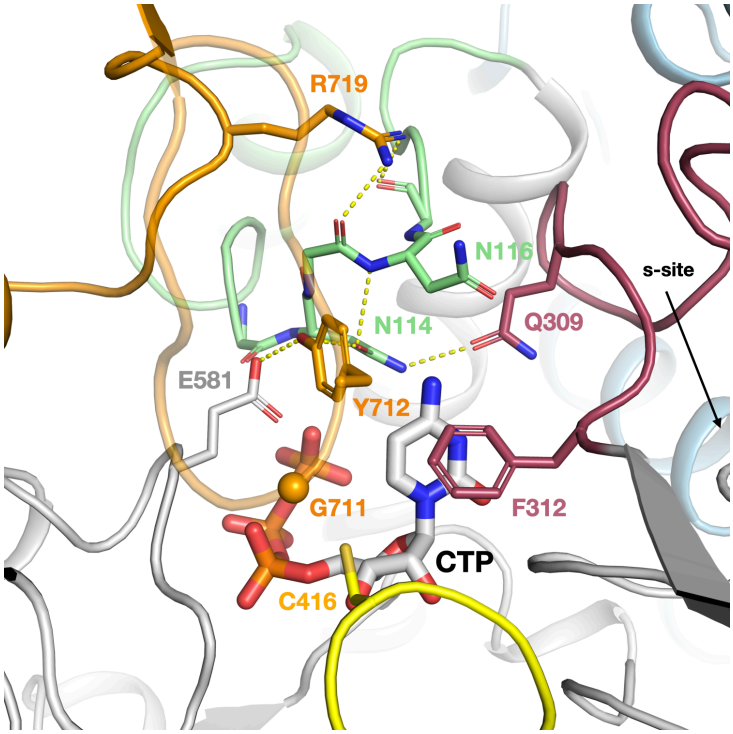

Figure 7: The intricate network of interactions between the NxN flap, C-terminal GRD, loop 2 and substrate in the ATP-CTP complex of PcNrdD. The NxN flap is coloured light green, the GRD orange, loop 2 dark red and the Cys radical loop yellow. The Gly radical loop is semi-transparent for clarity. The CA atom of Gly711 is indicated by an orange sphere. Important hydrogen bonds are shown as dotted lines.

As the NxN flap appears to close off the top of the active site, we used the web server Caver Web v1.1 (Stourac *et al*, 2019) to analyse substrate access to the active site in the ATP-bound form, and identified a tunnel ~12 Å long leading from the surface of the protein to the active site that is 5.6 Å in diameter at its narrowest point (Figure 7 - figure supplement 1). Thus, in principle a fresh substrate could diffuse into the active site on each catalytic cycle.

Cryo-EM structure of the ATP-dTTP-GTP dimer

In order to probe the generality of the conformations observed in the ATP-CTP complex, we also solved the structure of PcNrdD in complex with ATP in the a-site, specificity effector dTTP in the s-site, and substrate GTP in the active site (c-site). Again, 2D classes show a predominantly dimeric form with no more than ~10% tetramers. From a set of 437 886 particles selected from 2D classes with the best apparent density for the ATP-cone region, we obtained a volume at 2.40 Å resolution for the dimer with C1 symmetry that was further improved using DeepEMhancer (Table 1; Table 1 - table supplement 2). dTTP is clearly visible in the s-site (Figure 8 - figure supplement 1a) as is GTP in the active site (Figure 8 - figure supplement 2). A Mg^{2+} ion can be modelled in the s-site, coordinated by Glu290 and all three phosphate groups of dTTP. A β-hairpin loop between residues 185-192 that is disordered in the ATP-CTP structure in the absence of an s-site nucleotide is here ordered, due to an H-bond to the 2'-OH group of dTTP. Readout of the s-site nucleotide's identity is achieved through an H-bond to Asn298 (Figure 8 - figure supplement 1).

Like the ATP-CTP complex, the ATP-dTTP-GTP complex can also be partitioned into an active and an inactive monomer. The ATP-cone region is very disordered, but the last helix of the ATP-cone in the active monomer can be traced back to residue 85 (Fig. 8a,b). The helix is not kinked at residue 91 as in the ATP-CTP dimer but forms an uninterrupted helix between residues 85-104. The volume for the ATP-cone region lies entirely on one side of the PcNrdD dimer axis, as is also apparent in some of the 2D classes (Figure 8 – figure supplement 3). The ATP-cone cannot be modelled in detail, but if the volume is contoured at very low level, there is almost enough density for one ATP-cone. Taken together, this suggests that there is one partially disordered ATP-cone and one completely disordered in the ATP-dTTP-GTP complex. In the active monomer, the NxN flap and entire C-terminus are ordered while in the inactive monomer, the entire assembly of linker and NxN flap up to residue 120 and the entire GRD are disordered.

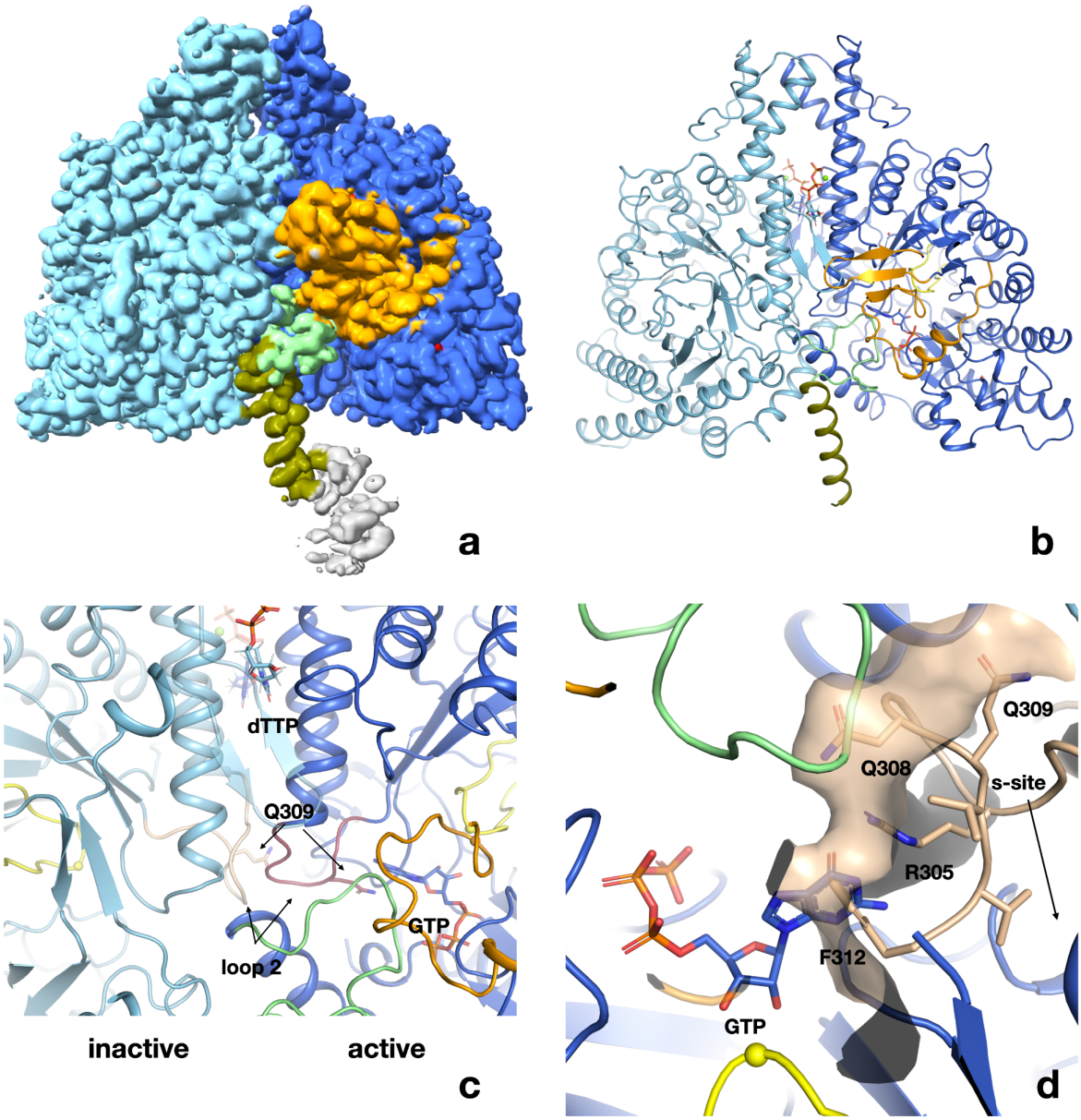

Figure 8. Structure of PcNrdD in complex with a-site effector ATP, s-site effector dTTP and substrate GTP. a) Volume for the PcNrdD dimer in complex with ATP, dTTP and GTP. The volume is contoured at a low level to emphasise the weak density for the more ordered ATP-cone domain in the active monomer. b) Ribbon diagram of the ATP-dTTP-GTP complex coloured as in Figure 6b, except that the most N-terminal helix (olive) now extends from residues 85-104. c) Zoom in on panel b) to illustrate the highly asymmetrical loop 2 conformations in the active and inactive monomers. Loop 2 in the inactive monomer (light blue) is

coloured dark blue, while in the active monomer (grey) it is dark red. The conformation of loop 2 that forms a complementary cradle for the guanosine base of the substrate GTP in the active monomer induces a conformation of the other loop 2 that precludes substrate binding. d) Severe steric clash of loop 2 of the inactive monomer with the substrate and NxN flap. The view is rotated approximately 180° from panels a-c. Loop 2 from the inactive monomer (wheat) is superimposed on the active site of the active monomer (dark blue). The molecular surface of the loop is shown to emphasise that this conformation is incompatible with an ordered NxN flap (light green) and substrate binding. The Cys radical loop is yellow and Cys416 is marked by a sphere. The Gly radical loop is omitted for clarity.

Intriguingly, binding of dTTP to the s-sites at the dimer interface induces two distinct conformations of loop 2 (Fig. 8c). In the active monomer, loop 2 is projected towards the aforementioned network of interactions between NxN flap, GRD and substrate, packing against the flap, though no polar interactions are apparent. However, loop 2 also makes extensive interactions with its equivalent in the inactive monomer, which forces the latter into a conformation where it would sterically clash with an ordered NxN flap (Fig. 8d). Furthermore, Phe412, which stacks on the substrate base in the active monomer, and Arg305, which is projected from the substrate-distal side of loop 2, sterically prevent the substrate binding in the inactive monomer. These may be important contributing factors to the disorder of the NxN flap and GRD. Finally, Gln309, which interacts with the substrate in the active monomer (Figure 8 - figure supplement 2), is oriented away from the substrate through its interactions with the “active” loop 2.

Cryo-EM structure of the ATP-dGTP dimer

As a third insight into the ATP-bound forms of PcNrdD, we solved the structure of PcNrdD in complex with specificity effector dGTP in the s-site and ATP at a concentration where it would both act as allosteric effector at the a-site and as the cognate substrate for dGTP (Table 1; Table 1 - table supplement 3). Density for dGTP is clearly visible in the s-site (Figure 8 - figure supplement 1d) and for ATP in the active site (Figure 8 - figure supplement 2). Again, the two monomers can be divided into an active one and an inactive one. The conformations of loop 2 are once again asymmetric (Figure 8 - figure supplement 4). The conformation in the active monomer is well-defined, while loop 2 in the inactive monomer is more flexible than in the ATP-dTTP-GTP complex, but still compatible with the hypothesis that the asymmetric arrangement of loop 2 is responsible for disorder of the NxN-GRD-substrate network in the inactive monomer.

Cryo-EM structure of the dATP-bound dimer

In micrographs of PcNrdD samples in the presence of 0.5 mM dATP, we observed an approximately 1:1 mixture of dimeric and tetrameric particles, consistent with results from GEMMA. To resolve whether dATP inhibition was linked to oligomerisation, we resolved the structures of each of these oligomers separately. We made a reconstruction of the dATP-bound PcNrdD dimer from 1 009 021 particles to 2.7 Å resolution that was further improved by DeepEMhancer postprocessing. The core domain is very similar to that of the ATP-CTP complex, with an rmsd in Cα positions of 1.2 Å for 1089 Cα atoms considering each dimer as a whole (Table 1; Table 1 - table supplement 4). dATP is clearly visible in the specificity site (Figure 8 - figure supplement 1b).

Strikingly, in contrast to the ATP complexes, the entire GRD is disordered in both monomers of the dATP-bound dimer. No structure is visible after residue 676 at the end of the last strand of the

barrel. This suggests that inhibition by binding of dATP to the ATP-cone is coupled to disordering of the C-terminal domain. The NxN flap that covers the top of the substrate in the ATP/CTP-bound form is also disordered, as are the ATP-cones themselves.

Cryo-EM structure of the dATP-bound tetramer

From the same micrographs that revealed the dATP-bound dimers we also resolved dATP-bound tetramers. We obtained a map from cryoSPARC at 2.8 Å, which was again improved with DeepEMhancer (Fig. 9a). Two dATP molecules are bound to each ATP-cone and one at each of the specificity sites, giving a total of 12 visible dATPs per tetramer. The tetramer reveals an arrangement of two dimers (chains A/B and C/D respectively) in which the ATP-cones are all well-ordered and one ATP-cone from each pair mediates interactions between the dimers (Fig. 9b). The ATP-cones have an almost domain-swapped arrangement within each dimer relative to the core domains. This oligomeric arrangement has not previously been observed within the RNR family.

dATP binds to the specificity site as in the dimeric dATP-bound form (Figure 8 - figure supplement 1c). The two dATP molecules bound to each ATP-cone do so very similarly to the dATP-loaded ATP-cones of the RNR class I active site subunit from PaNrdA (PDB ID 5IM3) and the class I radical generating subunit from LbNrdB (5OLK) to which the PcNrdD ATP-cones have 29% and 33% sequence identity respectively (Figure 9 – figure supplement 1). The DALI server reveals an rmsd in Cα positions of 1.9 Å and 1.7 Å respectively. The next most similar ATP-cone is that of the RNR transcriptional regulator NrdR from *Streptomyces coelicolor* in its dodecameric form (Rozman Grinberg *et al.*, 2022) binding two ATP molecules, with 82 aligned residues, rmsd 2.4 Å and sequence identity 17%. Structural similarity to other ATP-cones is listed in Figure 9 – figure supplement 1.

The two dATP molecules bind with their negatively charged triphosphate moieties oriented towards each other (Fig. 9c). No Mg^{2+} ion is observed between the triphosphate tails, but this may be an artefact of the cryo-EM method, as the PaNrdA and LbNrdB crystal structures suggest that this ion is necessary for charge neutralisation. As in the ATP-bound form, further charge compensation is achieved by extensive coordination by, or proximity of, basic side chains, e.g. Lys7, Arg8, Arg87 and Arg91. As previously observed in PaNrdA and LbNrdB, the adenosine base of the "inner" dATP (dATP1) fits into a pocket under the β-hairpin roof of the ATP-cone and the base of the "outer" nucleotide (dATP2) is sandwiched between an aromatic residue (Tyr83) and the side of the first α-helix in the domain. No direct contacts are seen between the dATP molecules bound to the ATP-cone and residues in the core domain.

Figure 9 – figure supplement 2 shows the differences in binding modes of dATP in the dATP-bound tetramer and ATP in the ATP-CTP dimer. The high mobility of the ATP-cone in the latter precludes a detailed analysis. However, it is clear that the triphosphate tails have very different orientations. In the ATP complex the tail of ATP2 is oriented away from the C-terminal helix towards the base of ATP1, such that the β-phosphate moiety may even H-bond to the base of ATP1. The side chain of Arg87 fills the space vacated by the γ-phosphate of ATP2. Instead of H-bonding to the γ-phosphate of ATP2, Arg91 swings away and interacts with the equivalent moiety of ATP2 in the ATP-cone of the other chain. The structures suggest that the additional 2'-OH

group in ATP may cause conformational changes in the ribose ring that propagate to the phosphate tail, but further analysis requires improved resolution.

As in PaNrdA and LbNrdB, the ATP-cones in the dATP-bound tetramer self-interact through a pair of α-helices at the C-terminal end of the ATP-cone. Remarkably, the pair of ATP-cones is highly asymmetrically positioned with respect to the 2-fold axis of its core dimer, being displaced as a rigid body towards the other dimer (Fig. 9b). Both pairs of ATP-cones are displaced in the same way, giving the complex overall C2 symmetry around an axis bisecting the pair of dimers. Consequently, the 2-fold axes of the ATP-cone and the core dimer are not aligned (Fig. 9b). The asymmetric arrangement is associated with two distinct conformations of the linker 93-103 between the fourth helix of the ATP-cone (Figure 9 – figure supplement 3a,b) and the core domain. In chains A and C, a small kink leads from helix 4 into a short helical segment that packs antiparallel to helix 122-142 in the core domain. In contrast, in chains B and D, the short helix is parallel to helix 122-142 and is joined to helix 4 at a 45° angle. The rest of the polypeptide between residues 103-121, including the NxN flap, is disordered in both linkers.

Interestingly, all contacts between the two dimers of the tetramer are mediated by interactions between one of the ATP-cones in one dimer (B or D) and one of the core domains of the other dimer (C or A respectively). Figure 9d shows the interactions of the roof of the ATP-cone with two outer helices from the C-terminal half of the barrel domain (residues 458-485 and 550-569, preceding the sixth and seventh strands). The interactions are mostly hydrophobic but are reinforced by several H-bonds, e.g. between Gln3D-Gln458A, Ser53D–Gln458A, Arg11D-Asp468A, the main chain amide of Ile12D and Tyr557A. The amount of buried surface area is small: 717 $Å^2$, or around 1% of the total surface area of each dimer. For comparison, the monomer-monomer interactions within each dimer bury 11.7 % of the total area. The residues on the core domain of PcNrdD involved in interactions with the ATP-cone of the other dimer do not show high sequence conservation, even when the alignments are restricted to the most similar sequences.

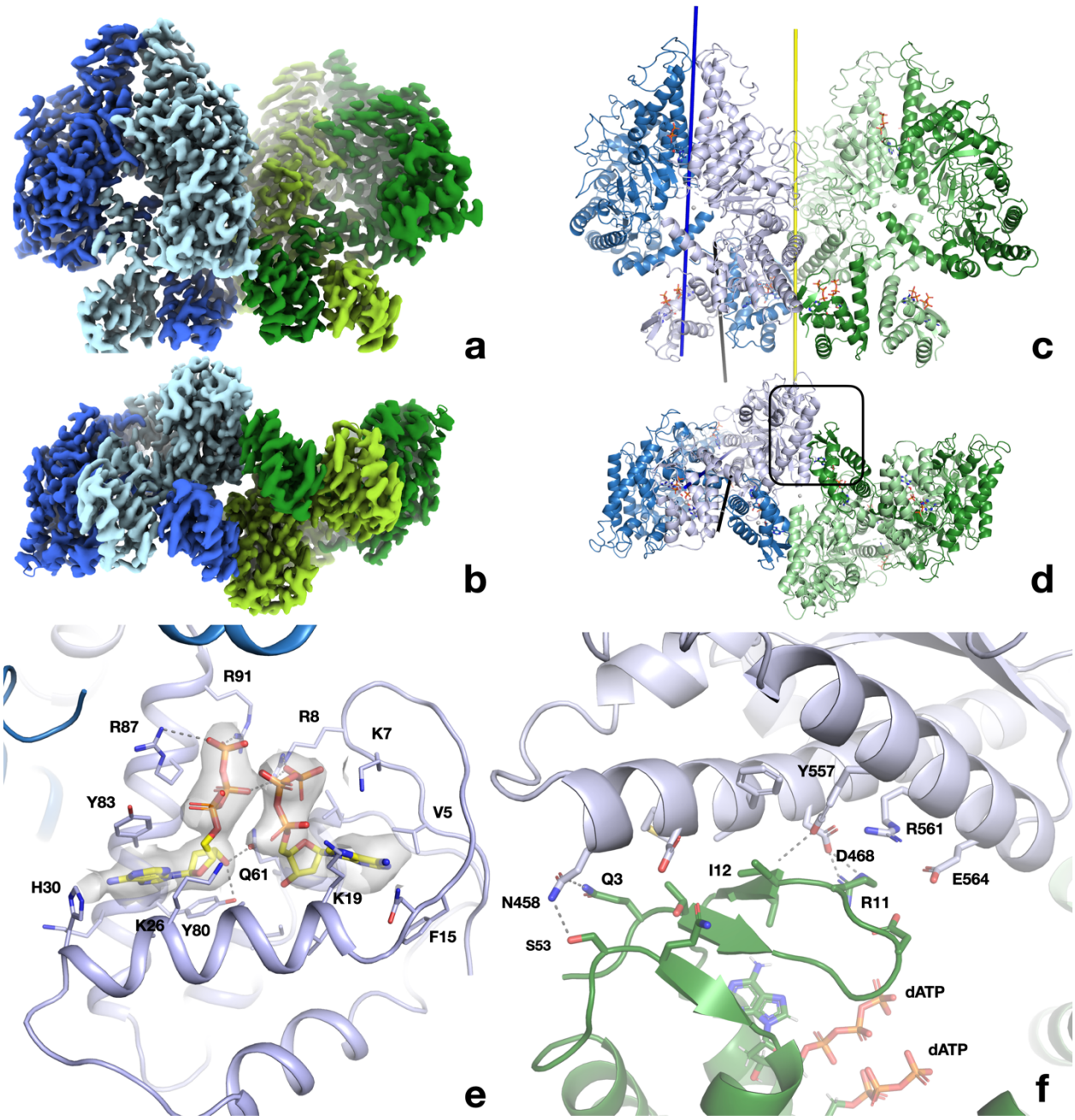

Figure 9: Structure of the dATP-bound PcNrdD tetramer. a) cryo-EM reconstruction coloured by chain: dimer 1 light blue and pale blue; dimer 2 light green and pale green. The four ATP-cones are at the bottom of the figure. b) View rotated by 90° around a horizontal axis relative to a) and thus viewed from the bottom, showing the ATP-cones. c-d) Cartoon representation of the tetramer from the same angles as panels a) and b) respectively and with the same chain colouring. The two-fold symmetry axis relating the two dimers of the tetramer is shown as a yellow line. The 12 dATP molecules in the tetramer are shown as sticks. The dimer axis of the left-hand dimer's core domains is shown as a dark blue line and the dimer axis of the ATP-cone pair as a black line. c) Details of the interaction of dATP molecules at the allosteric activity site in the ATP-cone. d) Close-up of the interaction area between the roof of the ATP-cone of one dimer and the core domain of the other dimer (marked with a black box in panel d). The most significant residues are labelled.

Cryo-EM structures of PcNrdD-dATP complexes produced in the presence of CTP

To investigate whether substrate had any allosteric effect on the conformations of the ATP-cone, flap and GRD, we determined separate cryo-EM structures of tetrameric and dimeric PcNrdD, from the same grid, in the presence of 0.5 mM dATP and 0.5 mM CTP, achieving a resolution of 2.6 Å from 1 105 348 particles before post-processing for the tetramer and 2.6 Å from 1 132 695 particles for the dimer (Table 1; Table 1 - table supplement 5). Both forms were almost identical to those seen in the presence of dATP alone, and no CTP could be seen bound to the active site (Figure 6 - figure supplement 2). This strongly suggests that substrate binding is dependent on ordering of the flap region by binding of ATP to the ATP-cone.

Discussion

Ribonucleotide reductase is an essential enzyme for all free-living organisms. Its complex regulation at the levels of transcription, overall activity and substrate specificity makes it quite unique in Nature (Mathews, 2016, 2018). A fundamental understanding of this regulation could e.g. pave the way for better antibiotics. The ATP-cone is a small, genetically mobile domain frequently found at the N-terminus of RNR catalytic subunits of all major classes, as well as in the bacterial RNR-specific transcription factor NrdR (Rozman Grinberg *et al.*, 2022). Its role in allosteric regulation of class I aerobic RNRs has been extensively studied. The ATP-cone mediates the formation of a surprising variety of different oligomeric complexes that nevertheless have in common that they block the formation of an (observed or inferred) active complex between the catalytic and radical generating subunits that permits proton-coupled electron transfer on each catalytic cycle (Martínez-Carranza *et al.*, 2020).

Despite their catalytic subunits being evolutionarily related to those of class I, anaerobic class III RNRs have a fundamentally different activation mechanism that is likely common to all glycyl radical enzymes (Backman *et al.*, 2017; Lundahl *et al*, 2022). Once generated on the catalytic subunit by encounter of the reductase with its radical SAM family activase, the glycyl radical can catalyse hundreds of cycles of turnover before being exhausted (Torrents *et al.*, 2001). Allosteric inhibition could thus in principle proceed by two mechanisms: by blocking the initial encounter of the reductase and activase, or by preventing subsequent transfer of the radical to the substrate. The first of these hypotheses is intuitively more similar to the steric blocking mechanisms encountered in class I RNRs; the latter is more challenging to understand, as the glycine and cysteine are buried in close proximity in the active site.

In this work we present the first biochemical, biophysical and structural characterisation of an anaerobic, class III RNR containing an ATP-cone, providing the first picture of the structural basis for allosteric activity regulation in this large family. We show that the ATP-cone can bind two molecules of ATP or dATP, but not both simultaneously. As expected, the presence of an ATP-cone confers inhibition of enzyme activity at high dATP concentrations. GEMMA experiments show that PcNrdD exists in a mixture of dimeric and tetrameric states under most experimental conditions studied, with the equilibrium shifted towards dimers in the presence of ATP. Addition of inhibiting concentrations of dATP shifts the equilibrium towards tetramers. The equilibria are not affected by substrate or specificity effector. EPR spectroscopy clearly shows that the glycyl radical is formed even in the presence of dATP. Together, these results show that dATP inhibition

in class III RNRs does not occur by blocking the initial encounter of reductase and activase. Instead, our nucleotide binding results show that dATP inhibition prevents binding of substrates.

The seven cryo-EM structures of PcNrdD in a variety of nucleotide complexes presented here suggest a mechanism in which binding of ATP or dATP modulates activity by affecting the degree of order of a tightly knit network of structural elements including the critical glycyl radical domain in the C-terminal region of the enzyme. In the presence of ATP and substrate CTP, the GRD is fully ordered in one monomer and Gly711 is found at its expected position proximal to Cys416, to which it will deliver its radical to initiate each catalytic cycle and accept it back at the end of the cycle. The CTP substrate is bound in this monomer and a conserved but previously unobserved flap containing two Asn residues (NxN flap) forms over the top of the substrate, making H-bonding interactions with it. Loop 2, which mediates between the substrate specificity site and the active site, is fully ordered. In contrast, in the other monomer, no substrate is bound, loop 2 is disordered and the flap and C-terminus are less well-ordered. At the same time, the ATP-cones themselves are relatively flexible. This is not unexpected for this type of ATP-cone, which binds two nucleotides and was first observed in the class I RNR PaNrdA (Johansson *et al.*, 2016). SAXS studies showed that the ATP-cone in PaNrdA is flexible in the presence of ATP, while in its dATP-bound form it forms a symmetric interaction with an ATP-cone on another dimer, causing the enzyme to tetramerise. A similar behaviour was seen even when this type of ATP-cone was evolutionarily "transplanted" to the N-terminus of the radical-generating subunit, as seen in LbNrdB (Rozman Grinberg *et al.*, 2018a).

By careful isolation of a subset of particles, we were able to characterise an unusual dimer of ATP-cones in the ATP-CTP complex, where four ATP molecules bind with all their triphosphate tails pointing towards each other. Such an orientation is unprecedented for RNRs, but such tail-to-tail orientations, compensated by extensive positive charges are found in e.g. adenylate kinases (Berry, 1994). The relevance of this arrangement remains to be elucidated. Interestingly, when dTTP was added to the s-site in the ATP-dTTP-CTP complex, the ATP-cones became much more disordered and could only be observed in one monomer of the dimer as diffuse density. This behaviour was reproduced with dGTP in the s-site. Both complexes with s-site effector are functionally more relevant forms than the ATP-CTP complex, as in the cell, a form with empty s-site is unlikely to exist. The partitioning of monomers into active and inactive is amplified by the presence of s-site effector (dTTP or dGTP) in both complexes with ATP. Only one of the active sites is occupied by substrate, with ordered NxN flap and C-terminal GRD. This is correlated with two distinct conformations of loop 2 in the two monomers. In the inactive monomer, the NxN flap and GRD are completely disordered as loop 2 obviates their ordering and concomitantly substrate binding. These results point to only one of the PcNrdD monomers being active at a given time and also to a significant cross-talk between the a-site, s-site and active site. This is corroborated by the finding that an s-site effector is necessary for retention of ATP by the ATP-cone when PcNrdD is first incubated with these nucleotides then purified without them.

In the presence of inhibitory concentrations of dATP we were able to isolate structures of both dimers and tetramers from the same cryo-EM sample, in agreement with the GEMMA results that show a shift towards the tetrameric form. In both forms, the C-terminal GRD is completely disordered in all monomers. In the tetramers, pairs of ATP-cones asymmetrically disposed relative to the 2-fold axes of their respective PcNrdD dimers associate through the “roof” of the “inner” dATP binding site to the core domain of the other dimer. While this allowed us to build complete models for the ATP-cones and analyse dATP binding, the role of tetramerisation in the inhibition

mechanism is unclear. The tetrameric structures appear to be facilitated by a dATP-induced "stiffening" of the pair of ATP-cones, similar to what was seen in PaNrdA and LbNrdB, and their interaction with a second dimer of PcNrdD, but the interaction area is small (1% of the total surface area) and the residues involved are not highly conserved in NrdDs, even from the most similar sequences. Furthermore, the GRD is disordered in all complexes with dATP in the a-site, whether dimeric or tetrameric. Since both the ATP-cone and the GRD are disordered in the dATP-bound dimers, the exact molecular mechanism by which dATP induces disorder of the GRD remains somewhat elusive.

Taken together, our results show a clear correlation between ATP or dATP binding to the ATP-cone and activity or inhibition respectively. The order-disorder transitions involve a previously uncharacterised but highly conserved structural element, the NxN flap, that folds over the substrate and furthermore acts as a structural bridge to the C-terminal GRD. Disordering of these elements prevents substrate binding and transfer of the radical from the GRD to the substrate. Interestingly, a similar flap is formed over the top of the active site in the *E. coli* active complex, but it is formed by part of the C-terminal region of the separate radical generating subunit (Kang, 2020). Thus, a locking of the substrate in the active site appears to be a conserved feature of active class I and class III RNRs. However, in class I RNR there is no tunnel allowing substrate access to the active site in the locked state. This is consistent with the fact that the class I subunits dissociate on each catalytic cycle, while in class III the glycyl radical can catalyse many substrate reductions before having to be regenerated. It remains enigmatic exactly how the tiny chemical difference between dATP and ATP (the 2'-OH group) results in such major conformational changes, as in the ATP-CTP complex, where the ATP-cones are visible, the a-site in the ATP-cone is separated from the NxN flap by at least 30 Å and in the most biologically relevant complexes with additional s-site effector, the ATP-cone is very disordered. Nevertheless, the present results give first insights into allosteric activity regulation in anaerobic RNRs and add yet another aspect to the surprisingly wide range of allosteric conformational changes that can be mediated by the binding of the two highly similar nucleotides ATP and dATP to a small, evolutionarily mobile protein domain.

Materials and Methods

Cloning of *nrdD* and *nrdG* from *P. copri*

The genes encoding the reductase (NrdD) and activase (NrdG) proteins from *P. copri* were synthesised by GenScript with codon optimization for *E. coli* and subcloned into the pBG102 plasmid (pET27 derivative) (Center for Structural Biology, Vanderbilt University) between the BamHI and EcoRI restriction sites to produce His6-SUMO-NrdD and His6-SUMO-NrdG protein constructs.

Overexpression and purification of PcNrdD and PcNrdG

Plasmids containing the *nrdD* gene or the *nrdG* gene were transformed into *E. coli* BL21 (DE3) star and *E. coli* BL21 (DE3) competent cells, respectively. Cells (6 L) were grown at 37 °C in Luria Broth supplemented with kanamycin (50 µg/mL) to an A_{600} of 1.2. Protein expression was then induced with 0.5 mM IPTG and incubation was extended overnight at 20 °C. After centrifugation, pellets were suspended in 60 mL of lysis buffer 1a (50 mM Tris-HCl pH 8, 500 mM KCl, 0.5 mM

TCEP) for PcNrdD and lysis buffer 2a (50 mM Tris-HCl pH 8, 500 mM NaCl, 0.5 mM TCEP) for PcNrdG, supplemented with lysozyme (0.5 mg/mL), and disrupted by sonication. Cell debris was removed by ultracentrifugation at 210 000 x g for 1 h at 4 °C. The supernatant was then loaded on an immobilised metal affinity Ni-NTA column (HisTrap 5 mL; Cytiva) equilibrated with buffer 1b (50 mM Tris-HCl, pH 8, 300 mM KCl) or buffer 2b (50 mM Tris-HCl, pH 8, 300 mM NaCl), supplemented with 50 mM imidazole as appropriate. The column was washed extensively with the corresponding buffer containing 50 mM imidazole and the His_6-SUMO tagged proteins were eluted using 300 mM imidazole. The proteins were collected and dialyzed overnight at 4 °C against buffer 1b or 2b supplemented with 1 mM 1,4-dithiothreitol (DTT) in the presence of the PreScission Protease (150 µM) to cleave the affinity-solubility tag. The GST–3C-protease (PreScission) was expressed using pGEX-2T recombinant plasmids. After induction at 25 °C with 0.1 mM IPTG for 20 h, the PreScission Protease was purified using glutathione–Sepharose chromatography. After the dialysis, the cleaved PcNrdD and PcNrdG proteins were centrifuged at 4 °C for 10 min and loaded onto a HisTrap column equilibrated with buffer 1b or 2b, supplemented with 50 mM imidazole and the flow-through containing the cleaved protein was collected. Following cleavage of the His_6-SUMO tag, the proteins incorporated a non-native N-terminal Gly-Pro-Gly-Ser sequence. The purified preparations are called as-purified PcNrdD and as-purified PcNrdG, respectively.

A fraction of as-purified PcNrdD was precipitated by addition of HCl, then centrifuged at 15 000 x g for 5 min. UV-visible spectra of the supernatant were recorded before and after protein precipitation to estimate the amount of nucleotide contamination. PcNrdD preparations with ≤5% nucleotide contamination are referred to as apo-PcNrdD.

Fractions containing apo-PcNrdD and as-purified PcNrdG were concentrated and loaded on a gel filtration column (Hiload 16/60 Superdex S200; Cytiva) in 25 mM Tris-HCl, pH 8, 250 mM NaCl, and 5 mM DTT. The purified protein was concentrated to 20 mg/mL with an Amicon ultrafiltration device (100 kDa cutoff for NrdD and 10 kDa cutoff for NrdG; Millipore), frozen in liquid nitrogen, and stored at −80 °C.

[Fe-S] cluster reconstitution and purification of holo-PcNrdG

The reconstitution of the [4Fe-4S] cluster and purification of PcNrdG containing an iron-sulfur cluster (holo-PcNrdG) were performed under strict anaerobic conditions in an Mbraun glove box kept at 18°C and containing less than 0.5 ppm O_2. PcNrdG was treated with 5 mM DTT for 10 min then incubated for 3 h with a fivefold molar excess of ferrous ammonium sulphate and L-cysteine in the presence of 2 µM *E. coli* cysteine desulfurase CsdA. The holo-PcNrdG was then loaded onto a Superdex 200 10/300 gel filtration column (Cytiva) equilibrated in 25 mM Tris-HCl, 250 mM NaCl, and 5 mM DTT. The peak containing the soluble holo-PcNrdG was then concentrated to 10 mg/mL on a Vivaspin concentrator (10 kDa cutoff) (Figure 1 - figure supplement 2).

In vitro enzymatic assay and HPLC analysis

Activity assays were performed under strict anaerobic conditions inside a glove box in 25 mM Tris pH 8, 50 mM KCl, 10 mM DTT in a volume of 100 µL. A standard pre-reaction mixture contained 1 µM apo-PcNrdD, 2.5 µM holo-PcNrdG, 500 µM *S*-adenosyl-methionine (SAM), 5 mM $MgCl_2$, 1 mM GTP (or 1 mM CTP), and different allosteric effectors dTTP, ATP or dATP. The pre-reaction

mixture was incubated for 5 min at 37 °C before adding simultaneously 10 mM sodium formate and sodium dithionite (12.5 molar excess). CTP was used as a substrate, ATP and dATP were titrated and when dTTP was used as an s-site effector, GTP was used as substrate.

The reaction was incubated for 10 min at 37 °C and stopped by the addition of 2.5 µL of 3 M formic acid. Product formation was analysed by HPLC using an Agilent ZORBAX RR StableBond (C18, 4.6 x 150 mm, 3.5 µm pore size) equilibrated with buffer A (10% methanol, 50 mM potassium phosphate buffer, pH 7, 10 mM tetrabutylammonium hydroxide). Samples of 10 µL were injected and eluted at 0.5 mL/min with a step isocratic flow of 40%-100% buffer B (30% methanol, 50 mM potassium phosphate buffer, pH 7, 10 mM tetrabutylammonium hydroxide). Compound identification and product quantification were performed by external calibration and NrdD specific activity was determined.

From a direct plot of activity versus concentration of effector, the K_L values for binding of effectors to the a-site, were calculated in KaleidaGraph using the equation:

$$V = V_{max} \times [dNTP]/(K_L + dNTP)$$

and K_i for non-competitive dATP inhibition was calculated in KaleidaGraph using the equation:

$$V = V_{max}/(1 + [dNTP]/K_i)$$

Isothermal titration calorimetry experiments

ITC experiments were carried out at 20°C on a MicroCal PEAQ-ITC system (Malvern Instruments Ltd) in a buffer containing 25 mM HEPES, pH 7.5, 100 mM KCl, 10 mM $MgCl_2$ and 0.5 mM TCEP with a stirring speed of 1000 rpm. An initial injection volume was 0.6 µl over a duration of 1.2 s. All subsequent injection volumes were 1.7–2.5 µl over 3.4–5 s with a spacing of 160 s between the injections. Data for the initial injection were not considered. PcNrdD was incubated with 1 mM dTTP, 1 mM GTP and 10 mM $MgCl_2$ at room temperature during 5 min. For dATP binding analysis, the concentration of PcNrdD in the cell was 50 to 100 µM and dATP concentration in the syringe 0.6 to 1 mM. For ATP titration into PcNrdD, protein concentration in the cell was 200 µM and ATP concentration in the syringe was 0.6 to 1.5 mM. The data were analysed using the one set of sites model of the MicroCal PEAQ-ITC analysis software (Malvern Panalytical). Standard deviations in thermodynamic parameters, N and K_D were estimated from the fits of three different titrations.

Microscale thermophoresis

Both binding of nucleotides to the ATP-cone in PcNrdD and binding of substrates CTP and GTP to PcNrdD were assessed using MST. PcNrdD was labelled using Monolith Protein Labeling Kit RED-NHS 2nd generation according to the manufacturer's protocol. MST was performed using the Monolith NT.115 instrument (NanoTemper Technologies GmbH) at room temperature. Binding of GTP and CTP was assayed in MST buffer containing 40 mM Hepes pH 7, 50 mM KCl, 50 and 100 mM $MgCl_2$, 5 mM DTT, 0.1% Tween-20, 1 mM dTTP (only for GTP binding) and either 5 mM ATP or 1 mM dATP. The 16 reaction tubes were prepared by the addition of 2 µl MST buffer (concentrated 5 times), 5 µl GTP or CTP of the desired concentration and 1 µl RED dye-labelled NrdD in a total volume of 10 µl. Final NrdD concentration in the binding reaction was 11 nM while the binding partner concentrations were between 70 mM and 2 µM for CTP and 50 mM and 1.5

μM for GTP. Binding of ATP and dATP to the ATP-cone was assayed in MST buffer containing 25 mM Hepes pH 7.5, 100 mM KCl, 10 mM $MgCl_2$, 0.5 mM TCEP, 0.1% Tween-20, 1 mM dTTP and 5 mM GTP. A 16-step dilution series of the binding partners was prepared by adding 5 μl buffer to 15 tubes. ATP or dATP was added to the first tube to the final concentration of 4 mM and 5 μl was transferred to the second tube and mixed by pipetting (1:1 dilution series). To each tube of the dilution series 5 μl of PcNrdD was added to reach a final concentration of 11 nM. The samples were transferred to Monolith™ NT.115 Series Premium Capillaries (NanoTemper Technologies GmbH), which were scanned using the MST instrument (100% excitation power, medium MST power). Obtained MST data was analysed and fitted using the MO. Affinity Analysis v2.3 software (NanoTemper Technologies) with default parameters. K_D and standard deviation for GTP and CTP binding to PcNrdD in the presence of ATP and for ATP and dATP binding to the ATP-cone were calculated using fits from at least three individual titrations. No binding was detected for CTP or GTP to PcNrdD in the presence of dATP.

Nucleotide binding to the PcNrdD ATP-cone

PcNrdD was incubated with nucleotides at room temperature for 30 minutes and then desalted on a NAP-5 column. The desalted protein was boiled for 10 min, centrifuged, and the supernatant was loaded on a Agilent ZORBAX RR StableBond (C18, 4.6 x 150 mm, 3.5 μm pore size) HPLC column to evaluate the amount of nucleotides retained by the protein. Samples of 100 μL were injected on the column equilibrated with buffer A (10% methanol, 50 mM potassium phosphate buffer, pH 7, 10 mM tetrabutylammonium hydroxide) and eluted at 1 mL/min with a gradient of 40%-100% buffer B (30% methanol, 50 mM potassium phosphate buffer, pH 7, 10 mM tetrabutylammonium hydroxide). Compound identification and product quantification were performed by comparison with injected standards. Three different sets of experiments were performed, each set consisting of incubation with only ATP, only dATP, and a combination of ATP and dATP. In the first set of experiments 75 μM apo-NrdD was incubated with 1 mM ATP or 1 mM dATP, and when 1 mM each of ATP and dATP was used, dATP was added 15 min after addition of ATP. After 30 min incubation the mixtures were desalted in a buffer without nucleotides. In the second set of experiments 75 μM apo-NrdD in presence of 1 mM dTTP and 5 mM GTP was incubated with 3 mM ATP or 1 mM dATP, and when both nucleotides were combined dATP was added 15 min after addition of ATP. After 30 min incubation the mixtures were desalted in a buffer without nucleotides. In the third set of experiments 75 μM apo-NrdD in presence of 2 mM dTTP and 5 mM GTP was incubated with 3 mM ATP or 1 mM dATP, and when both nucleotides were combined dATP was added 15 min after addition of ATP. After 30 min incubation the mixtures were desalted in a buffer containing 0.1 mM dTTP and 1 mM GTP. It was possible to separate all phosphorylation levels of adenosine and deoxyadenosine nucleotides in the first set of experiments, but not in the second and third sets due to overlapping peaks of the s-site and substrate nucleotides (Figure 2 - figure supplement 1).

Gas-phase electrophoretic mobility molecular analysis

The GEMMA instrumental setup and general procedures were as described previously (Kaufman *et al.*, 1996; Rofougaran *et al*, 2008). Apo-PcNrdD was equilibrated into a buffer containing 100 mM ammonium acetate pH 7.8, then applied onto a Sephadex G-25 chromatography column. In addition, 5 mM DTT was added to the PcNrdD protein solution to increase the protein stability. Prior to analysis, the protein sample was diluted to 2 μM in a buffer containing 100 mM ammonium acetate, pH 7.8, 0.005% (v/v) Tween 20, magnesium acetate (equimolar to the total nucleotide

concentration) and the corresponding nucleotides (where indicated). The protein samples were then incubated for 2 min at room temperature, centrifuged and applied to the GEMMA instrument for data collection. The experiments were performed with a flow rate driven by 2 psi to minimise noise signals that may appear with elevated nucleotide or protein concentrations at the manufacturer's recommended flow rate driven by 3.7 psi.

Glycyl radical characterization by EPR

EPR samples were handled under strictly anaerobic conditions inside a glovebox in 25 mM Tris-HCl pH 8, 50 mM KCl, 5 mM DTT in a final volume of 100 µL. A standard pre-reaction mixture containing 75 µM holo-PcNrdG, 1 mM *S*-adenosyl-methionine, was treated with a 12.5 excess of dithionite and was incubated for 20 min at 37 °C. The pre-mixture was added to a mixture of 50 µM apo-PcNrdD, 10 mM sodium formate, supplemented or not with 1.5 mM ATP or 1 mM dATP and in the presence of 1 mM CTP. The final reaction was incubated for 20 min at 37 °C and 100 µL sample was transferred into a standard EPR tube (Wilmad LabGlass 707-SQ-250M) and stored in liquid nitrogen before recording the EPR spectrum.

X-band CW-EPR spectra of PcNrdD were recorded on a Bruker ELEXYS-E500 spectrometer operating at microwave frequency of 9.38 GHz, equipped with a SuperX EPR049 microwave bridge and a cylindrical TE_{011} ER 4122SHQE cavity in connection with an Oxford Instruments continuous flow cryostat. Measuring temperature at 30 K was achieved using liquid helium flow through an ITC 503 temperature controller (Oxford Instruments). For achieving non-saturating conditions, a microwave power of 10 µW was applied for all measurements. Other EPR settings were: modulation frequency of 100 kHz; modulation amplitude of 8 G; and accumulation of 16 scans for an optimal S/N ratio. Double integrated spectra were used for intensity analysis.

Cryo-EM sample preparation and data acquisition

The proteins for cryo-EM analysis were all prepared in the same manner. Apo-PcNrdD was incubated with 1 mM NTP or dNTP at room temperature for 5 min, then centrifuged before injection onto a Superdex S200 10/300 column pre-equilibrated with a buffer containing 25 mM HEPES-NaOH pH 7.5, 100 mM KCl, 0.5 mM TCEP, 10 mM $MgCl_2$ and supplemented with varying concentrations of 0.5 mM NTP or 0.2 mM dNTP. The relevant peak was collected, then diluted at 0.5 mg/mL and the corresponding nucleotides were added to different final concentrations (0.5-5 mM NTP or 0.5-1 mM dNTP) (Table 1).

The grids were glow-discharged for 60 s at 20 mA using a GloQube (Quorum) instrument, then prepared in the following manner: 3 µL of sample at 0.5 mg/ml were applied on Quantifoil 1.2, 1.3 300 mesh Cu grids or Quantifoil 2.1, 300 mesh Au grids and plunge-frozen in liquid nitrogen-cooled liquid ethane using a Vitrobot Mark IV (Thermo Fisher Scientific) with a blot force of 1 and followed by 5 s blot time, at 4 °C and 100% humidity. The grids used for each sample are specified in Table 1.

Grids were clipped and loaded into a 300 kV Titan Krios G2 microscope (Thermo Fisher Scientific, EPU 2.8.1 software) equipped with a Gatan BioQuantum energy filter and a K3 Summit direct electron detector (AMETEK). Grids were screened for quality based on particle distribution and density, and images from the best grid were recorded. Micrographs were recorded at a nominal

magnification of 105,000. Details of the other data collection parameters used for each sample are given in Table 1.

Cryo-EM data processing

Data processing was performed in cryoSPARC (Punjani *et al*, 2017). The first steps in processing of all datasets were patch motion correction and patch CTF estimation, followed by curation of exposures based on ice thickness, poor defocus estimation, etc. Other steps are as detailed below. Resolution estimation in cryoSPARC was done using a gold standard Fourier shell correlation value of 0.143 (Rosenthal & Henderson, 2003). Map post-processing was done using DeepEMhancer (Sanchez-Garcia *et al.*, 2021) and post-processing resolution estimation was performed using DeepRes (Ramirez-Aportela *et al*, 2019). Models were placed in the maps using either phenix.dock_in_map (Liebschner *et al*, 2019) or Molrep (Vagin & Teplyakov, 1997) in the CCP-EM package (Burnley *et al*, 2017). Model building was done by alternating rounds of manual building in Coot (Emsley *et al*, 2010) with real space refinement in phenix.refine (Liebschner *et al.*, 2019). Secondary structure restraints were used throughout. The inclusion of riding hydrogen atoms reduced the number of bad contacts in all models. An AlphaFold2 (Jumper *et al.*, 2021) model of PcNrdD was used in the later stages of building the first model to resolve some ambiguous loops. All final models have good correlations between map and model and good stereochemical properties (Table 1). All structures have been deposited in the Protein Databank and the corresponding volumes deposited in the Electron Microscopy Data Bank with the accession numbers listed in Table 1.

PcNrdD-ATP-CTP complex

Data processing: A total of 17 033 movies were used after curation. A low-pass filtered volume was made in Chimera (Pettersen *et al*, 2021) from the crystal structure of NrdD from *T. maritima* (TmNrdD, PDB ID 4COI). From this volume, a set of templates was created and used for template-based picking with a diameter of 100 Å. Due to the large number of micrographs, they were split into two sets. The largest set (16 219 micrographs) was analysed first. About 8.6 million particles were extracted with a 350-pixel box size and classified into 60 2D classes. Eight representative classes containing different orientations (~3.3 million particles) were used to generate four ab-initio models without symmetry (C1) and particles were subjected to three-dimensional (3D) heterogeneous refinement using four classes. The most populated model containing ~1 million particles was subjected to homogeneous and non-uniform refinement, which gave a map with an overall FSC resolution of 2.94 Å. A further 435 695 particles were then extracted from the remaining 810 micrographs. These were subjected to 2D classification, and the resulting classes were merged with the larger set, giving 1 199 575 particles. The combined particles were subjected to homogeneous, non-uniform refinement and local refinement with a predefined mask, which gave a map at 2.87 Å (Table 1 - table supplement 1).

Generation of map with better ATP-cone density: The particles were further classified into 50 2D classes, from which 23 classes having 1 040 266 particles were selected. Four ab-initio models were generated and 570 730 particles with slightly better ATP-cone density were refined without symmetry. The particles were then subjected to 3D classification using ten classes of ~57 000 particles each. The classes having slightly better ATP-cone density were selected for further processing and final refinement without symmetry gave a map with an overall FSC resolution of 3.17 Å from 291 231 particles, which was post-processed using DeepEMhancer (Table 1 - table supplement 1).

Model building and refinement: A partially complete model for one dimer of the dATP complex (see below) was placed in the map using phenix.dock_in_map. The ATP-cones were built based on the ones from the dATP-only tetramers (see below).

PcNrdD-dATP complexes

Tetramers

Data processing for first part: A set of 11 161 movies was used after curation, template-based picking based on the structure of TmNrdD and particle extraction using a box size of 448 pixels gave 5 331 420 particles. Seven 2D classes having 1 171 839 particles were used to make ab-initio models, followed by heterogeneous refinement. The best class having 461 020 particles and volume was used for homogeneous refinement, which gave a map at 3.3 Å. Non-uniform refinement followed by local refinement with a pre-determined mask gave a map at 3.1 Å with no imposed symmetry.

Data processing for second part: A set of 16 667 movies was used after curation. Particles were picked and extracted using the same box size as in the first part, which gave 7 889 234 particles. Ten 2D classes having 1 881 057 particles were used to make two ab-initio models, followed by heterogeneous refinement. The best class with 1 083 657 particles was selected and subjected to homogeneous refinement followed by non-uniform refinement and a local new refinement with a pre-determined mask, which gave a map at 2.9 Å with no imposed symmetry.

Merging of datasets and CTF refinement: The best particles from the first dataset were classified into 80 2D classes from which 36 having 399 523 particles were selected. The particles from the second dataset resulting in the best volume were classified into 100 2D classes, of which 31 having 949 610 particles were selected. These particle sets were merged (giving 1 349 133 particles) and refined against the best 3D volume which gave a map at 2.78 Å. Iterative refinement and NU refinement jobs, ultimately using C2 symmetry, and local CTF refinement with a defocus search range of +/- 2000, gave a map at 2.8 Å with C2 symmetry that was post-processed using DeepEMhancer (Table 1 - table supplement 4).

Model building and refinement: Model building was initially done for one dimer by fitting a homology model generated using SwissModel with T4NrdD as a template to the map using phenix.dock_in_map. Similar homology models for the four ATP-cones were placed by hand into the density followed by rounds of real space refinement. After almost completely rebuilding one dimer, the second dimer was placed into the density and model building and refinement were continued.

Dimers

The first part of the data processing was shared with the PcNrdD-dATP tetramers. In the same micrographs there were a number of 2D class averages that represented dimers. Eight such class averages having 1 916 387 particles were used to make two ab-initio models. This was followed by rounds of heterogeneous refinement from where the best model having 1 009 021 particles was refined with no symmetry to give a map at 2.8 Å. A final non-uniform refinement with C1 symmetry gave a map at 2.6 Å that was post-processed using DeepEMhancer (Table 1 - table supplement 4).

PcNrdD-dATP-CTP complexes

Tetramers

Blob picking was carried out from 11 780 curated micrographs with a maximum diameter of 200 Å and a minimum diameter of 90. In total 4 646 479 particles were then extracted with a box size of 448 pixels. This was followed by 2D classification, ab-initio model generation and heterogeneous refinements. The best class with 1 105 348 particles was used for non-uniform refinement with C2 symmetry, which gave a final map at 2.59 Å resolution that was post-processed using DeepEMhancer (Table 1 - table supplement 5).

Dimers

The initial data processing steps were the same as above. Template based picking from 8 796 curated micrographs using a low-pass filtered volume of the dATP-only tetramer gave 6 836 668 particles after extraction with a box size of 300 pixels. This was followed by 2D classifications, selection of classes representing dimers, ab-initio model generations and refinement of the best class. The final round of non-uniform refinement with 1 132 695 particles with C1 symmetry gave a map of 2.53 Å resolution. The estimated median resolution after post-processing was 2.1 Å (Table 1 - table supplement 5). Model building used the coordinates of the dATP-only dimer as a starting model.

PcNrdD-ATP-dTTP-GTP complex

Data processing: A total of 12 501 movies were processed and 6 105 movies were used after curation. Template-based picking was used with a diameter of 150 pixels. About 3.9 million particles were extracted from 5 952 movies with a 400 pixel box size and used for two-dimensional (2D) classification into 100 classes. Eleven representative 2D classes containing different orientations (~2.4 million particles) were used to generate an ab-initio model and particles were subjected to three-dimensional (3D) heterogeneous refinement using ten classes, resulting in the most populated model containing 437 866 particles. This model was subjected to homogeneous and non-uniform refinement, which gave a map with an overall FSC resolution of 2.47 Å. The particles were then subjected to 3D classification and the resulting classes were merged for further processing and final refinement without symmetry (C1) gave a map with an overall FSC resolution of 2.4 Å that was post-processed using DeepEMhancer (Table 1 - table supplement 2).

Model building and refinement: A complete model for the dimer of the ATP-CTP structure (see above) was placed in the map using phenix.dock_in_map. The ATP-cones were removed as they were not visible in the reconstruction. After model building and refinement, the final map-to-model correlation value was X. Model quality statistics are presented in Table 1.

PcNrdD-ATP-dGTP complex

Data processing: Template-based picking was carried out on 14 373 curated micrographs and 4 522 028 particles were extracted with a box size of 350 pixels. This was followed by multiple rounds of 2D classifications, ab-initio model generation and refinements. C1 symmetry was applied on the best volume which gave a map with 589 345 particles having a final resolution of 2.58 Å. Model building and refinement used the PcNrdD-ATP/CTP complex as a starting model. (Table 1 - table supplement 3)

Bioinformatics

To construct an HMM logo of NrdD sequences, a representative selection of NrdD sequences from all domains of life including viruses were collected and aligned with Clustal Omega (Sievers *et al*, 2011). Subsequently an HMM model was built with hmmbuild from the HMMER suite (Eddy, 2011) and a logo was created using the Skylign web service using the "Information Content - Above Background" option (Wheeler *et al*, 2014). Conserved parts of the logo were extracted and displayed here.

Acknowledgements

We dedicate this article to PhD candidate Ipsita Banerjee¶ who made seminal contributions to the data processing parts of this study but who passed away suddenly on 7th December 2022. The authors thank Gustav Berggren, Uppsala University, Martin Högbom, Stockholm University, and Marc Fontecave, Collège de France, for letting us use their anaerobic chambers, Anders Hofer, Umeå University, for the GEMMA instrument, David Drew and Henrietta Nielsen, Stockholm University, for the ITC and the MST instruments, Anders Olsson, SciLifeLab Stockholm University, for the ITC and HPLC instruments, Annette Roos, SciLifeLab Uppsala University, for her help during the procedure of NrdD labelling for MST, Alexey Pisarev and Thomas Jonsen, Agilent, for fixing our HPLC instrument, and Malvern Panalytical for kindly sharing the MicroCal PEAQ-ITC analysis software for the analysis of ITC data. We would like to also thank master student Sina Becker for size exclusion chromatography experiments. Cryo-EM sample screening, optimization, and data collection were performed at the Cryo-EM Swedish National Facility, funded by the Knut and Alice Wallenberg, Family Erling Persson and Kempe Foundations, SciLifeLab, Stockholm University and Umeå University. The authors would like to thank Marta Carroni, Karin Walldén, Julian Conrad, Terezia Kovalova and Victor Tobiasson for their assistance during the cryo-EM experiments. This study was supported by grants from the Swedish Research Council (2019-01400 to BMS, 2016–04855 to DTL), the Swedish Cancer Society (CAN 20 1210 PjF to BMS), and the Wenner-Gren Foundations (to BMS).

References

Andersson J, Westman M, Hofer A, Sjöberg BM (2000) Allosteric regulation of the class III anaerobic ribonucleotide reductase from bacteriophage T4. *J Biol Chem* 275: 19443-19448. doi: 10.1074/jbc.M001490200

Ando N, Brignole EJ, Zimanyi CM, Funk MA, Yokoyama K, Asturias FJ, Stubbe J, Drennan CL (2011) Structural interconversions modulate activity of *Escherichia coli* ribonucleotide reductase. *Proc Natl Acad Sci U S A* 108: 21046-21051. doi: 10.1073/pnas.1112715108

Ando N, Li H, Brignole EJ, Thompson S, McLaughlin MI, Page JE, Asturias FJ, Stubbe J, Drennan CL (2016) Allosteric inhibition of human ribonucleotide reductase by dATP entails the stabilization of a hexamer. *Biochemistry* 55: 373-381. doi: 10.1021/acs.biochem.5b01207

Aravind L, Wolf YI, Koonin EV (2000) The ATP-cone: an evolutionarily mobile, ATP-binding regulatory domain. *J Mol Microbiol Biotechnol* 2: 191-194.

Aurelius O, Johansson R, Bågenholm V, Lundin D, Tholander F, Balhuizen A, Beck T, Sahlin M, Sjöberg BM, Mulliez E *et al* (2015) The crystal structure of *Thermotoga maritima* class III ribonucleotide reductase lacks a radical cysteine pre-positioned in the active site. *PLoS One* 10: e0128199. doi: 10.1371/journal.pone.0128199

Backman LRF, Funk MA, Dawson CD, Drennan CL (2017) New tricks for the glycyl radical enzyme family. *Crit Rev Biochem Mol Biol* 52: 674-695. doi: 10.1080/10409238.2017.1373741

Berry MB, Meador B, Bilderback T, Liang P, Glaser M, Phillips GN, Jr. (1994) The closed conformation of a highly flexible protein: the structure of E. coli adenylate kinase with bound AMP and AMPPNP. *Proteins* 19: 183-198. doi: 10.1002/prot.340190304

Birgander PL, Kasrayan A, Sjöberg BM (2004) Mutant R1 proteins from Escherichia coli class Ia ribonucleotide reductase with altered responses to dATP inhibition. *J Biol Chem* 279: 14496-14501. doi: 10.1074/jbc.M310142200

Brignole EJ, Tsai KL, Chittuluru J, Li H, Aye Y, Penczek PA, Stubbe J, Drennan CL, Asturias F (2018) 3.3-A resolution cryo-EM structure of human ribonucleotide reductase with substrate and allosteric regulators bound. *Elife* 7: e31502. doi: 10.7554/eLife.31502

Burnim AA, Spence MA, Xu D, Jackson CJ, Ando N (2022a) Comprehensive phylogenetic analysis of the ribonucleotide reductase family reveals an ancestral clade. *Elife* 11: e79790. doi: 10.7554/eLife.79790

Burnim AA, Xu D, Spence MA, Jackson CJ, Ando N (2022b) Analysis of insertions and extensions in the functional evolution of the ribonucleotide reductase family. *Protein Sci* 31: e4483. doi: 10.1002/pro.4483

Burnley T, Palmer CM, Winn M (2017) Recent developments in the CCP-EM software suite. *Acta Crystallogr D Struct Biol* 73: 469-477. doi: 10.1107/s2059798317007859

Crona M, Avesson L, Sahlin M, Lundin D, Hinas A, Klose R, Söderbom F, Sjöberg BM (2013) A rare combination of ribonucleotide reductases in the social amoeba *Dictyostelium discoideum*. *J Biol Chem* 288: 8198-8208. doi: 10.1074/jbc.M112.442434

Eddy SR (2011) Accelerated profile HMM searches. *PLoS Comput Biol* 7: e1002195. doi: 10.1371/journal.pcbi.1002195

Eliasson R, Pontis E, Sun X, Reichard P (1994) Allosteric control of the substrate specificity of the anaerobic ribonucleotide reductase from *Escherichia coli*. *J Biol Chem* 269: 26052-26057. doi: 10.1016/S0021-9258(18)47158-X

Emsley P, Lohkamp B, Scott WG, Cowtan K (2010) Features and development of Coot. *Acta Crystallogr D Biol Crystallogr* 66: 486-501. doi: 10.1107/S0907444910007493

Fairman JW, Wijerathna SR, Ahmad MF, Xu H, Nakano R, Jha S, Prendergast J, Welin RM, Flodin S, Roos A *et al* (2011) Structural basis for allosteric regulation of human ribonucleotide reductase by nucleotide-induced oligomerization. *Nat Struct Mol Biol* 18: 316-322. doi: 10.1038/nsmb.2007

Hofer A, Crona M, Logan DT, Sjöberg BM (2012) DNA building blocks: keeping control of manufacture. *Crit Rev Biochem Mol Biol* 47: 50-63. doi: 10.3109/10409238.2011.630372

Holm L (2022) Dali server: structural unification of protein families. *Nucleic Acids Res* 50: W210-W215. doi: 10.1093/nar/gkac387

Högbom M, Sjöberg BM, Berggren G (2020) Radical Enzymes. In: *eLS*, pp. 375-393. doi: 10.1002/9780470015902.a0029205

Johansson R, Jonna VR, Kumar R, Nayeri N, Lundin D, Sjöberg BM, Hofer A, Logan DT (2016) Structural mechanism of allosteric activity regulation in a ribonucleotide reductase with double ATP cones. *Structure* 24: 906-917. doi: 10.1016/j.str.2016.03.025

Jonna VR, Crona M, Rofougaran R, Lundin D, Johansson S, Brännström K, Sjöberg BM, Hofer A (2015) Diversity in overall activity regulation of ribonucleotide reductase. *J Biol Chem* 290: 17339-17348. doi: 10.1074/jbc.M115.649624

Jumper J, Evans R, Pritzel A, Green T, Figurnov M, Ronneberger O, Tunyasuvunakool K, Bates R, Zidek A, Potapenko A *et al* (2021) Highly accurate protein structure prediction with AlphaFold. *Nature* 596: 583-589. doi: 10.1038/s41586-021-03819-2

Kang G, Taguchi AT, Stubbe J, Drennan CL (2020) Structure of a trapped radical transfer pathway within a ribonucleotide reductase holocomplex. *Science* 368: 424-427. doi: 10.1126/science.aba6794

Kaufman SL, Skogen JW, Dorman FD, Zarrin F, Lewis KC (1996) Macromolecule analysis based on electrophoretic mobility in air: globular proteins. *Anal Chem* 68: 1895-1904. doi: 10.1021/ac951128f

Larsson KM, Andersson J, Sjöberg BM, Nordlund P, Logan DT (2001) Structural basis for allosteric substrate specificity regulation in anaerobic ribonucleotide reductases. *Structure* 9: 739-750. doi: 10.1016/s0969-2126(01)00627-x

Liebschner D, Afonine PV, Baker ML, Bunkoczi G, Chen VB, Croll TI, Hintze B, Hung LW, Jain S, McCoy AJ *et al* (2019) Macromolecular structure determination using X-rays, neutrons and electrons: recent developments in Phenix. *Acta Crystallogr D Struct Biol* 75: 861-877. doi: 10.1107/S2059798319011471

Logan DT, Andersson J, Sjöberg BM, Nordlund P (1999) A glycyl radical site in the crystal structure of a class III ribonucleotide reductase. *Science* 283: 1499-1504. doi: 10.1126/science.283.5407.1499

Lundahl MN, Sarksian R, Yang H, Jodts RJ, Pagnier A, Smith DF, Mosquera MA, van der Donk WA, Hoffman BM, Broderick WE *et al* (2022) Mechanism of radical S-adenosyl-l-methionine adenosylation: radical intermediates and the catalytic competence of the 5'-deoxyadenosyl radical. *J Am Chem Soc* 144: 5087-5098. doi: 10.1021/jacs.1c13706

Lundin D, Berggren G, Logan DT, Sjöberg BM (2015) The origin and evolution of ribonucleotide reduction. *Life (Basel)* 5: 604-636. doi: 10.3390/life5010604

Martínez-Carranza M, Jonna VR, Lundin D, Sahlin M, Carlson LA, Jemal N, Högbom M, Sjöberg BM, Stenmark P, Hofer A (2020) A ribonucleotide reductase from *Clostridium botulinum* reveals distinct evolutionary pathways to regulation via the overall activity site. *J Biol Chem* 295: 15576-15587. doi: 10.1074/jbc.RA120.014895

Mathews CK (2016) The most interesting enzyme in the world. *Structure* 24: 843-844. doi: 10.1016/j.str.2016.05.006

Mathews CK (2018) Still the most interesting enzyme in the world. *FASEB J* 32: 4067-4069. doi: 10.1096/fj.201800790R

Mulliez E, Ollagnier S, Fontecave M, Eliasson R, Reichard P (1995) Formate is the hydrogen donor for the anaerobic ribonucleotide reductase from Escherichia coli. *Proc Natl Acad Sci U S A* 92: 8759-8762. doi: 10.1073/pnas.92.19.8759

Ormö M, Sjöberg BM (1990) An ultrafiltration assay for nucleotide binding to ribonucleotide reductase. *Anal Biochem* 189: 138-141. doi: 10.1016/0003-2697(90)90059-i

Pettersen EF, Goddard TD, Huang CC, Meng EC, Couch GS, Croll TI, Morris JH, Ferrin TE (2021) UCSF ChimeraX: Structure visualization for researchers, educators, and developers. *Protein Sci* 30: 70-82. doi: 10.1002/pro.3943

Punjani A, Rubinstein JL, Fleet DJ, Brubaker MA (2017) cryoSPARC: algorithms for rapid unsupervised cryo-EM structure determination. *Nat Methods* 14: 290-296. doi: 10.1038/nmeth.4169

Ramirez-Aportela E, Mota J, Conesa P, Carazo JM, Sorzano COS (2019) DeepRes: a new deep-learning- and aspect-based local resolution method for electron-microscopy maps. *IUCrJ* 6: 1054-1063. doi: 10.1107/S2052252519011692

Rofougaran R, Crona M, Vodnala M, Sjöberg BM, Hofer A (2008) Oligomerization status directs overall activity regulation of the *Escherichia coli* class Ia ribonucleotide reductase. *J Biol Chem* 283: 35310-35318. doi: 10.1074/jbc.M806738200

Rosenthal PB, Henderson R (2003) Optimal determination of particle orientation, absolute hand, and contrast loss in single-particle electron cryomicroscopy. *J Mol Biol* 333: 721-745. doi: 10.1016/j.jmb.2003.07.013

Rozman Grinberg I, Lundin D, Hasan M, Crona M, Jonna VR, Loderer C, Sahlin M, Markova N, Borovok I, Berggren G *et al* (2018a) Novel ATP-cone-driven allosteric regulation of ribonucleotide reductase via the radical-generating subunit. *Elife* 7: e31529. doi: 10.7554/eLife.31529

Rozman Grinberg I, Lundin D, Sahlin M, Crona M, Berggren G, Hofer A, Sjöberg BM (2018b) A glutaredoxin domain fused to the radical-generating subunit of ribonucleotide reductase (RNR) functions as an efficient RNR reductant. *J Biol Chem* 293: 15889-15900. doi: 10.1074/jbc.RA118.004991

Rozman Grinberg I, Martínez-Carranza M, Bimai O, Nouairia G, Shahid S, Lundin D, Logan DT, Sjöberg BM, Stenmark P (2022) A nucleotide-sensing oligomerization mechanism that controls NrdR-dependent transcription of ribonucleotide reductases. *Nat Commun* 13: 2700. doi: 10.1038/s41467-022-30328-1

Sanchez-Garcia R, Gomez-Blanco J, Cuervo A, Carazo JM, Sorzano COS, Vargas J (2021) DeepEMhancer: a deep learning solution for cryo-EM volume post-processing. *Commun Biol* 4: 874. doi: 10.1038/s42003-021-02399-1

Sievers F, Wilm A, Dineen D, Gibson TJ, Karplus K, Li W, Lopez R, McWilliam H, Remmert M, Soding J *et al* (2011) Fast, scalable generation of high-quality protein multiple sequence alignments using Clustal Omega. *Mol Syst Biol* 7: 539. doi: 10.1038/msb.2011.75

Stourac J, Vavra O, Kokkonen P, Filipovic J, Pinto G, Brezovsky J, Damborsky J, Bednar D (2019) Caver Web 1.0: identification of tunnels and channels in proteins and analysis of ligand transport. *Nucleic Acids Res* 47: W414-W422. doi: 10.1093/nar/gkz378

Torrents E, Buist G, Liu A, Eliasson R, Kok J, Gibert I, Gräslund A, Reichard P (2000) The anaerobic (class III) ribonucleotide reductase from *Lactococcus lactis*. Catalytic properties and allosteric regulation of the pure enzyme system. *J Biol Chem* 275: 2463-2471. doi: 10.1074/jbc.275.4.2463

Torrents E, Eliasson R, Wolpher H, Gräslund A, Reichard P (2001) The anaerobic ribonucleotide reductase from *Lactococcus lactis*. Interactions between the two proteins NrdD and NrdG. *J Biol Chem* 276: 33488-33494. doi: 10.1074/jbc.M103743200

Torrents E, Westman M, Sahlin M, Sjöberg BM (2006) Ribonucleotide reductase modularity: Atypical duplication of the ATP-cone domain in *Pseudomonas aeruginosa*. *J Biol Chem* 281: 25287-25296. doi: 10.1074/jbc.M601794200

Vagin A, Teplyakov A (1997) MOLREP: an Automated Program for Molecular Replacement. *J Appl Crystallogr* 30: 1022-1025. doi: doi:10.1107/S0021889897006766

Wei Y, Funk MA, Rosado LA, Baek J, Drennan CL, Stubbe J (2014) The class III ribonucleotide reductase from *Neisseria bacilliformis* can utilize thioredoxin as a reductant. *Proc Natl Acad Sci U S A* 111: E3756-3765. doi: 10.1073/pnas.1414396111

Wheeler TJ, Clements J, Finn RD (2014) Skylign: a tool for creating informative, interactive logos representing sequence alignments and profile hidden Markov models. *BMC Bioinformatics* 15: 7. doi: 10.1186/1471-2105-15-7

Tables

Table 1: Data collection, processing, and refinement statistics for the cryo-EM structures of PcNrdD

ligands	dATP tetramer	dATP dimer	ATP-dTTP-GTP dimer	ATP-dGTP dimer	ATP-CTP dimer	dATP-CTP tetramer	dATP-CTP dimer
PDB entry	8P28	8P27	8P2S	8P39	8P23	8P2C	8P2D
EMDB entry	EMD-17359	EMD-17358	EMD-17373	EMD-17385	EMD-17357	EMD-17360	EMD-17361
Concentrations (mM)	0.5		5.0 / 1.0/ 1.0	5.0 / 1.0	0.5 / 0.5	0.5 / 0.5	0.5 / 0.5
grids	Quantifoil 1.2/1.3, 300 mesh Cu		Quantifoil 2.1, 300 mesh Au	Quantifoil 2.1, 300 mesh Au	Quantifoil 2.1, 300 mesh Cu	Quantifoil 2.1, 300 mesh Cu	Quantifoil 2.1, 300 mesh Cu
pixel size (Å)	0.8676		0.824	0.860	0.8676	0.8464	
dose rate (e^-/px/s)	16.1		15.0	15.0	17.1	13.7	
exposure time (s)	2.0		2.0	2.0	2.1	2.0	
Total dose (e^-/Å^2)	46		40	40	48	38	
defocus range (μM)	-1.0 to -3.4		-0.8 to -2.2	-0.6 to -2.4	-0.6 to -2.4	-0.6 to -2.0	
micrographs used (collected)	16,667 (21,804)		4,964 (12,501)	14,346 (16,745)	17,033 (21,512)	11,780 (15,268)	8,796 (15,268)
particles in final class	1,349,133	1,009,021	437,866	589,345	291,231	1,105,348	1,132,695
symmetry	C2	C1	C1	C1	C1	C2	C1
Resolution (FSC = 0.143; Å)	2.77	2.73	2.40	2.56	3.17	2.59	2.59
map sharpening B-factor (Å^2)	138.5	128.0	70.5	72.3	152.8	107.8	108.9
CC(mask) from phenix.refine	0.76	0.77	0.76	0.63	0.74	0.81	0.64
Model composition							
non-hydrogen atoms (residues)	21,141 (2,584)	8,710 (1,089)	9,694 (1,201)	9,705 (1,200)	11,399 (1,401)	21,137 (2,584)	8,793 (1,087)
ligands	8 dATP (a)	2 dATP (s)	2 dTTP (s)	2 dGTP (s)	4 ATP (a) 1 CTP (c)	8 dATP (a) 4 dATP (s)	2 dATP (s)

	4 dATP (s)		1 GTP (c)	1 ATP (c)			
min/mean/max B-factors protein (Å^2)	52.8 / 63.4 / 84.7	40.2 / 50.6 / 66.6	25.6 / 35.4 / 72.9	12.6 / 41.2 / 98.7	15.7 / 66.1 / 124.4	15.5 / 49.4 / 136.4	30.9 / 43.6 / 78.1
min/mean/max B-factors ligands (Å^2)	55.8 / 62.9 / 74.5	47.1 / 47.2 / 47.4	25.4 / 33.1 / 79.3	10.8 / 33.1 / 88.0	26.0 / 81.2 / 123.7	18.0 / 46.8 / 92.7	35.9 / 36.2 / 47.2
Deviations from ideal geometry							
rmsd (bonds)	0.005	0.004	0.003	0.003	0.004	0.004	0.002
rmsd (angles)	0.61	0.55	0.54	0.60	0.58	0.59	0.51
Ramachandran plot (%)							
favoured	90.1	91.7	95.2	93.8	93.8	94.1	92.0
allowed	9.9	8.3	4.7	5.8	5.9	5.9	8.0
outliers	0.0	0.0	0.1	0.4	0.3	0.0	0.0
rotamer outliers	1.9	5.4	3.0	6.0	3.8	4.2	4.8
MolProbity score	2.1	2.4	2.2	2.5	2.2	2.3	2.5
MolProbity clash score	6.5	6.2	8.7	10.0	5.5	7.1	10.2

Supplementary materials

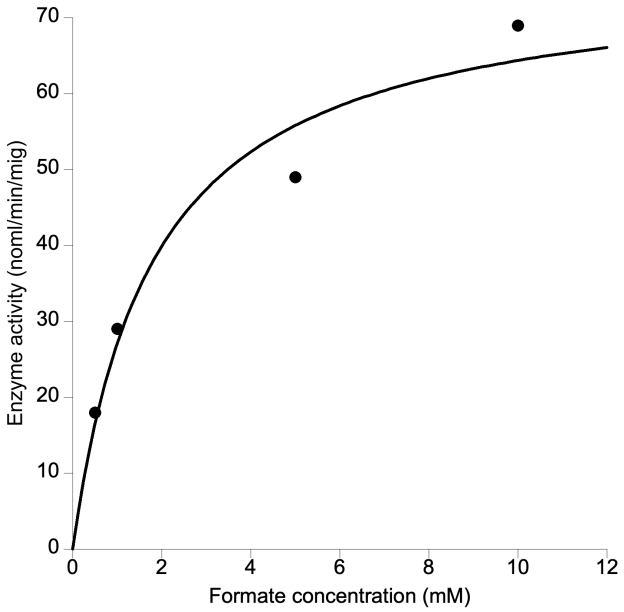

Figure 1 - figure supplement 1. Formate requirement in PcNrdD. KaleidaGraph curve fit using the Michaelis-Menten equation.

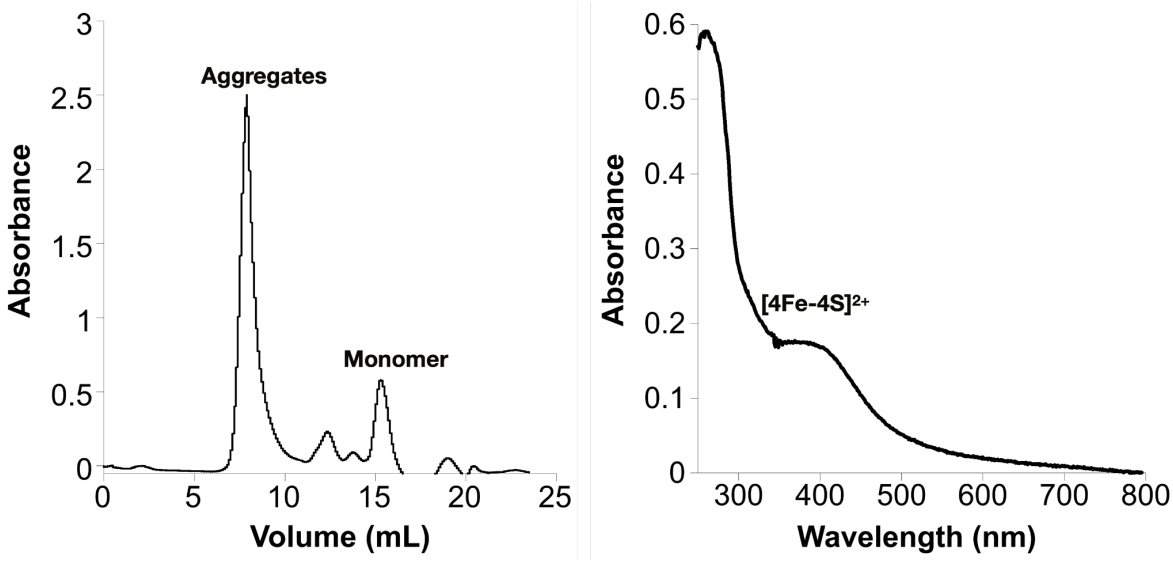

Figure 1 - figure supplement 2. Reconstitution of the [Fe-S] cluster of the *Prevotella copri* NrdG. (a) Reconstituted holo-PcNrdG loaded in a Superdex S200 10/300. (b) UV-visible spectrum of the holo-PcNrdG.

Figure 2 - figure supplement 1. Amount of ATP and/or dATP bound to PcNrdD during different incubation and desalting conditions.

Incubating conditions	Desalting conditions	ATP (mol/mol NrdD)	dATP (mol/mol NrdD)
NrdD+ATP[a]	No nucleotides during desalting	0.09[k]	0
NrdD+dATP[b]		0	0.97[l]
NrdD+ATP+dATP[c]		0.01	0.89[m]
NrdD+ATP+dTTP+GTP[d]	No nucleotides during desalting	0.03	0.01
NrdD+dATP+dTTP+GTP[e]		0	0.64
NrdD+ATP+dATP+dTTP+GTP[f]		0.01	1
NrdD+ATP+dTTP+GTP[g]	dTTP+GTP included during desalting[j]	0.35	0
NrdD+dATP+dTTP+GTP[h]		0	0.52
NrdD+ATP+dATP+dTTP+GTP[i]		0.05	0.85

[a]1 mM ATP, [b]1 mM dATP, [c]1 mM ATP, 1mM dATP, [d]3 mM ATP, 1 mM dTTP, 5 mM GTP, [e]1 mM dATP, 1 mM dTTP, 5 mM GTP, [f]3 mM ATP, 1 mM dATP, 1 mM dTTP, 5 mM GTP, [g]3 mM ATP, 2 mM dTTP, 5 mM GTP, [h]1 mM dATP, 2 mM dTTP, 5 mM GTP, [i]3 mM ATP, 1 mM dATP, 2 mM dTTP, 5 mM GTP, [j]0.1 mM dTTP, 1 mM GTP, [k]Summary of 0.07 mol/mol NrdD ATP and 0.02 mol/mol NrdD ADP, [l]Summary of 0.78 mol/mol NrdD dATP, 0.18 mol/mol NrdD dADP, and 0.01 mol/ molNrdD dAMP, [m]Summary of 0.70 mol/mol NrdD dATP, 0.18 mol/mol NrdD dADP, and 0.01 mol/mol NrdD dAMP.

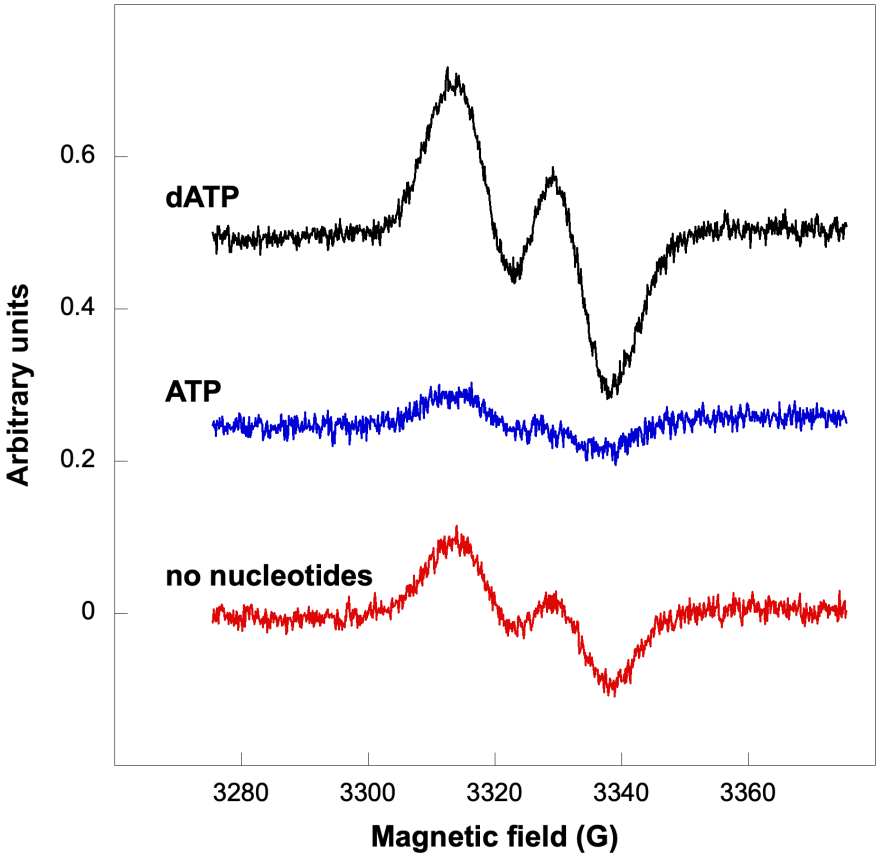

Figure 4 - figure supplement 1. Glycyl radical formation in absence of formate after 20 min incubation. Nucleotide concentrations were: ATP 1.5 mM and dATP 1 mM. Traces are arbitrarily moved to increase visibility and scaled to identical units (Y-axes).

Figure 6 - figure supplement 1. Structural similarity comparisons to overall PcNrdD. Structural similarity tables from DALI (PDB90, i.e. targets filtered at 90% sequence identity)

PDB ID	Protein	Z-score	Residues aligned	RMSD (Å)	Sequence identity (%)
1H7A	Bacteriophage T4 NrdD	34.6	535	2.5	27
4U3E	*T. maritima* NrdD	25.5	508	3.0	16
4COL	*T. maritima* NrdD / dATP	24.8	493	2.9	17

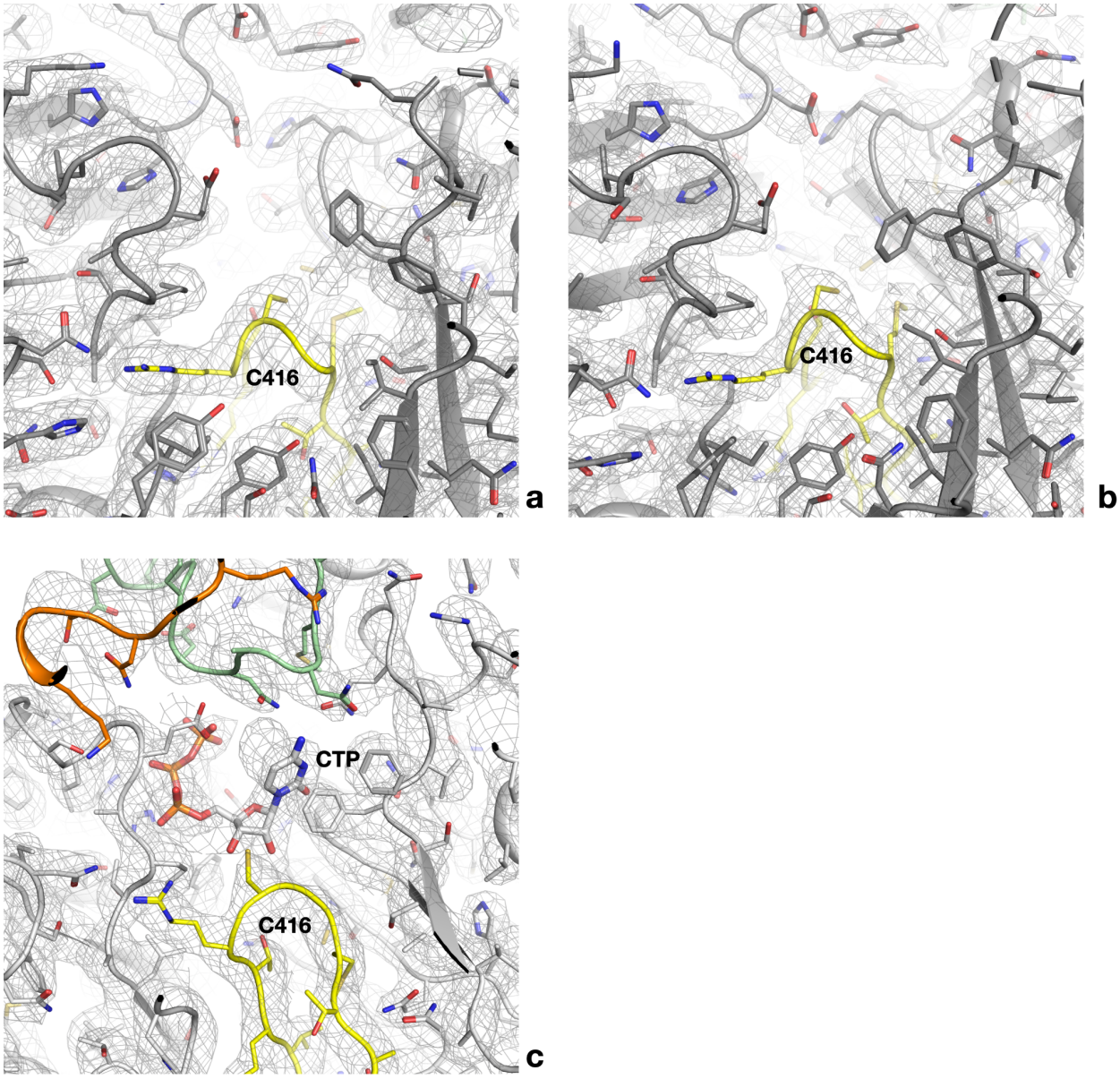

Figure 6 - figure supplement 2. a) Cryo-EM map for one of the four active sites of the dATP-CTP tetramer. The refined model is superposed. All side chains are shown as sticks. The finger loop is coloured yellow. b) Map for one of the two active sites of the dATP-CTP dimer. c) Complete density for the occupied active site of the ATP-CTP complex for comparison. The NxN flap is coloured green and the C-terminal region orange.

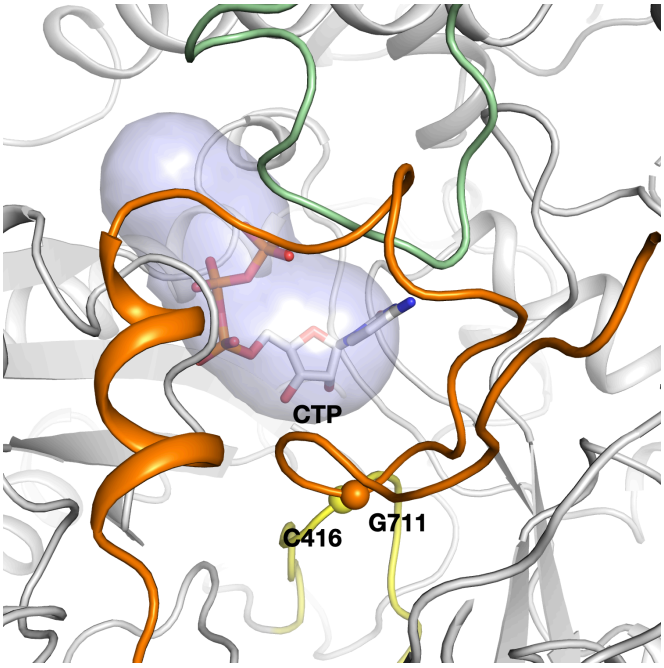

Figure 7 - figure supplement 1. The tunnel leading from the active site to the surface of PcNrdD in the ATP-CTP complex. The tunnel is 12 Å in length and 5.6 Å wide at its narrowest point. The secondary structure elements are coloured as in Figure 6.

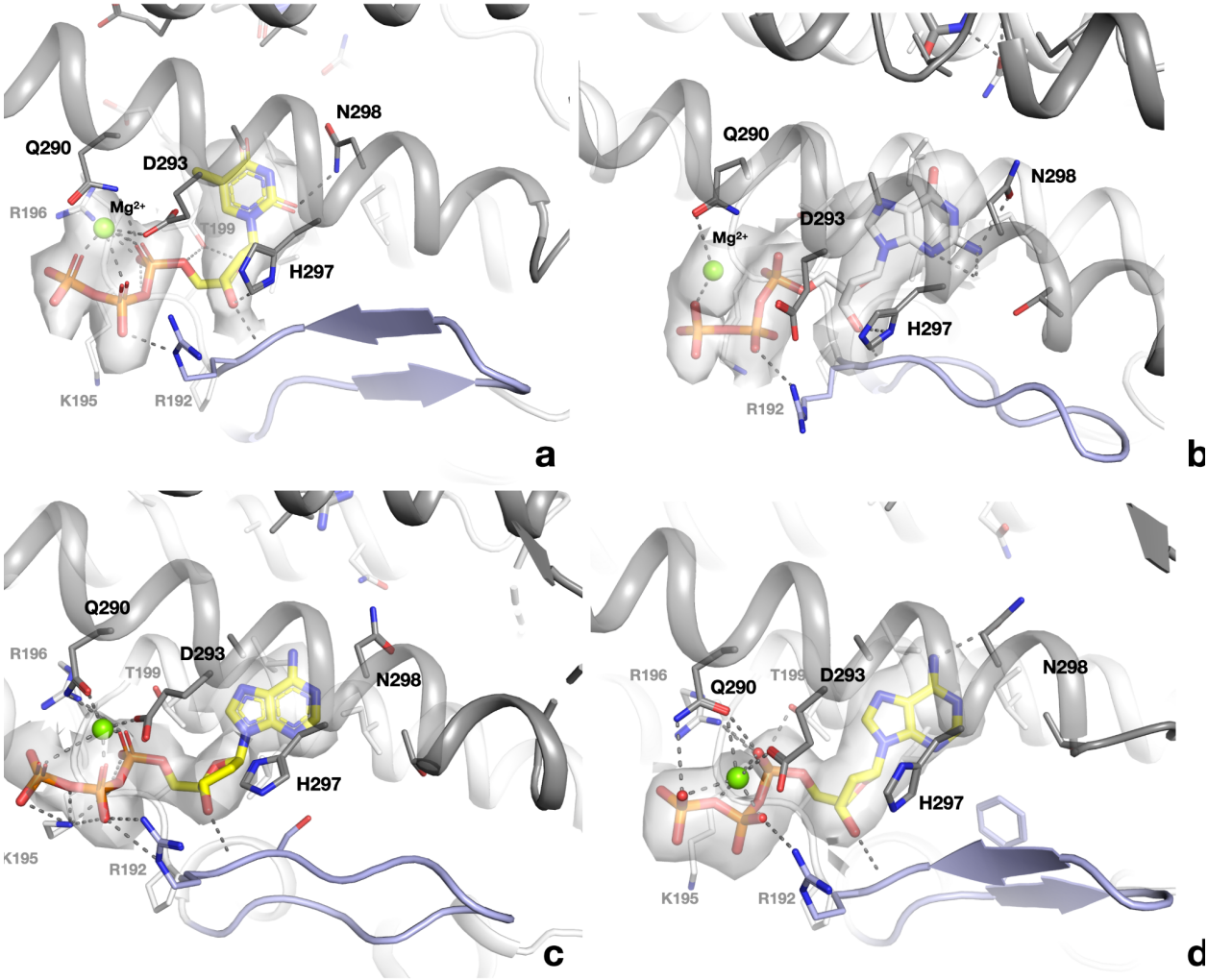

Figure 8 - figure supplement 1. Binding of allosteric substrate specificity nucleotides to the s-site at the dimer interface of PcNrdD. a) dTTP in the ATP-dTTP-GTP dimer; b) dGTP in the dGTP-ATP dimer; c) dATP in the dATP-only tetramer; d) dATP in the dATP-only dimer. Electrostatic potential maps are shown as transparent surfaces around the nucleotides. Residues in the monomer that makes most contacts to the nucleotide are indicated with black labels, residues in the other monomer with grey labels.

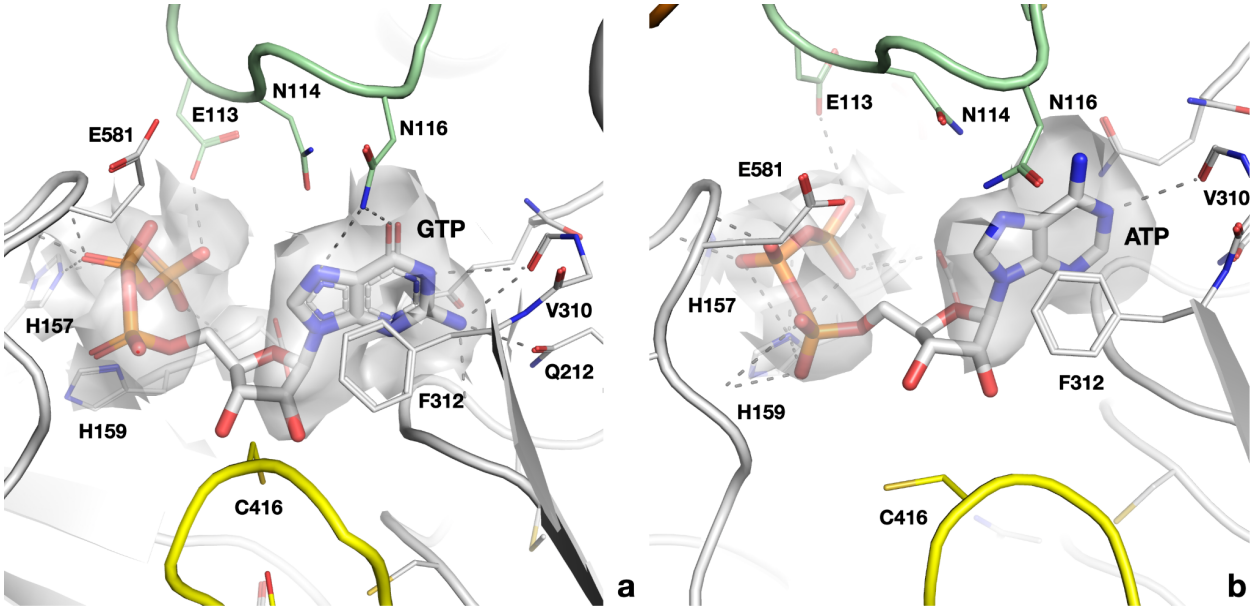

Figure 8 - figure supplement 2. Cryo-EM map and interactions of a) GTP in the active site of the PcNrdD-ATP-dTTP-GTP complex; b) ATP in the PcNrdD-ATP-dGTP complex

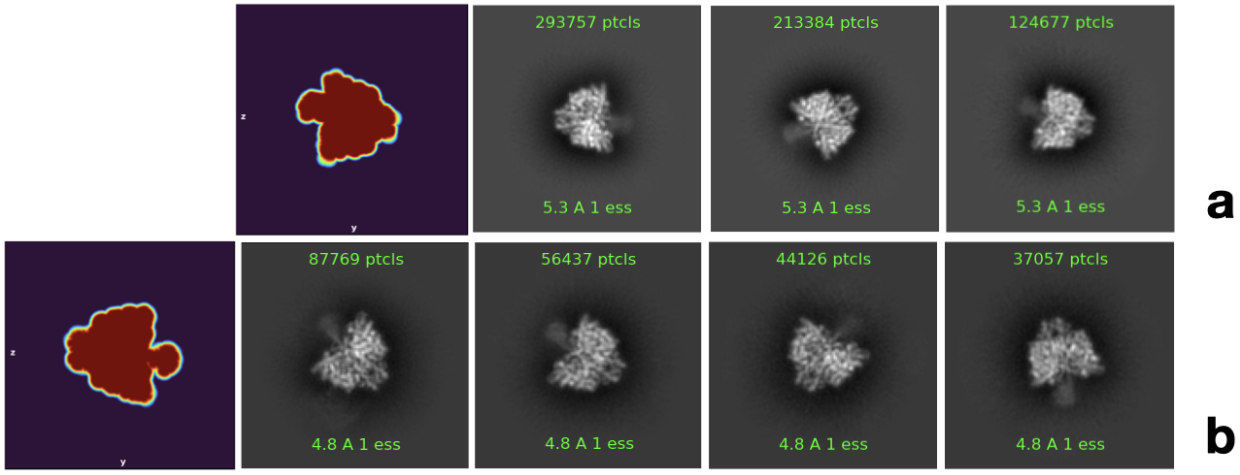

Figure 8 - figure supplement 3: Representative 2D classes showing side views of PcNrdD with diffuse density in the ATP-cone region. a) 3 classes for the complex with ATP, dTTP and GTP; b) 4 classes from the complex with ATP and dGTP. In both complexes the diffuse density appears limited to one side of the dimer axis. The left-hand panel in both a) and b) shows one projection of the automatically-determined masks used in the respective final non-uniform refinement jobs, which has the same form as the representative 2D classes.

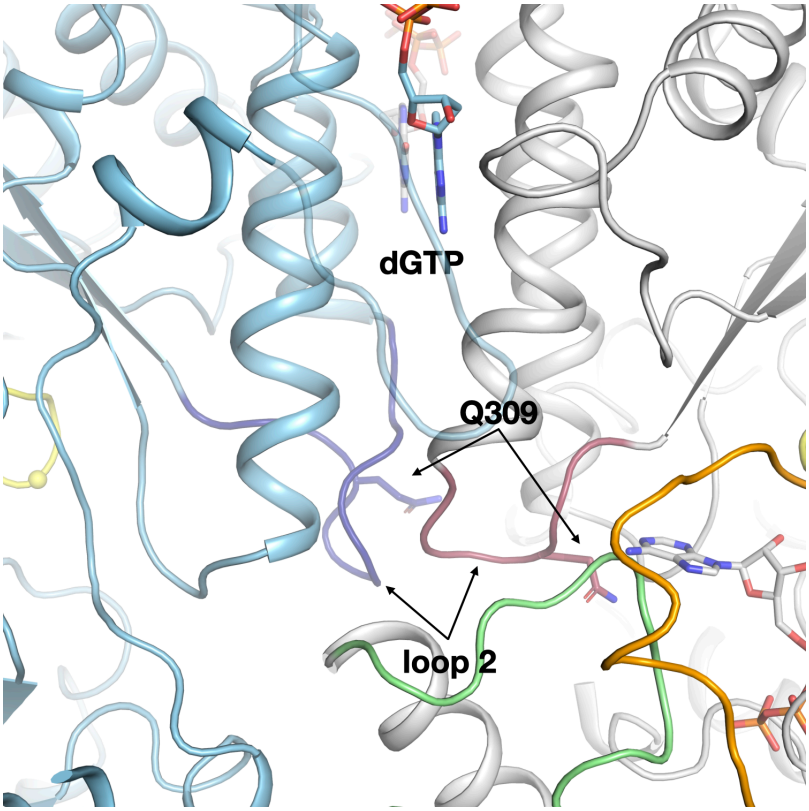

Figure 8 - figure supplement 4. The highly asymmetrical loop 2 conformations in the active and inactive monomers of the PcNrdD-dGTP-ATP complex. Loop 2 in the inactive monomer (light blue) is coloured dark blue, while in the active monomer (grey) it is dark red. As in the PcNrdD-ATP-dTTP-GTP complex, the conformation of loop 2 that forms a complementary cradle for the guanosine base of the substrate ATP in the active monomer induces a conformation of the other loop 2 that precludes substrate binding.

Figure 9 - figure supplement 1. Structural similarity comparisons to PcNrdD ATP-cone alone. The PcNrdD ATP-cone in the comparison is the one from the dATP tetramer structure.

PDB ID	Protein	No. of bound nucleotides	Z-score	Residues aligned	RMSD (Å)	Sequence identity (%)
5IM3	*P. aeruginosa* NrdA	2 dATP	12.2	92	1.9	29
5OLK	*L. blandensis* NrdB	2 dATP	12.1	93	1.7	33
7P37	*S. coelicolor* NrdR	2 ATP	10.0	82	2.4	17
6AUI	Human NrdA / dATP	1 dATP	9.5	88	2.8	19
7AGJ	*A. aeolicus* NrdA / ATP	2 ATP	8.7	88	2.2	17
5R1R	*E. coli* NrdA E441A	–	8.2	88	3.3	16
7MDI	*N. gonorrhoeae* NrdA	1 dATP	7.4	87	3.4	16

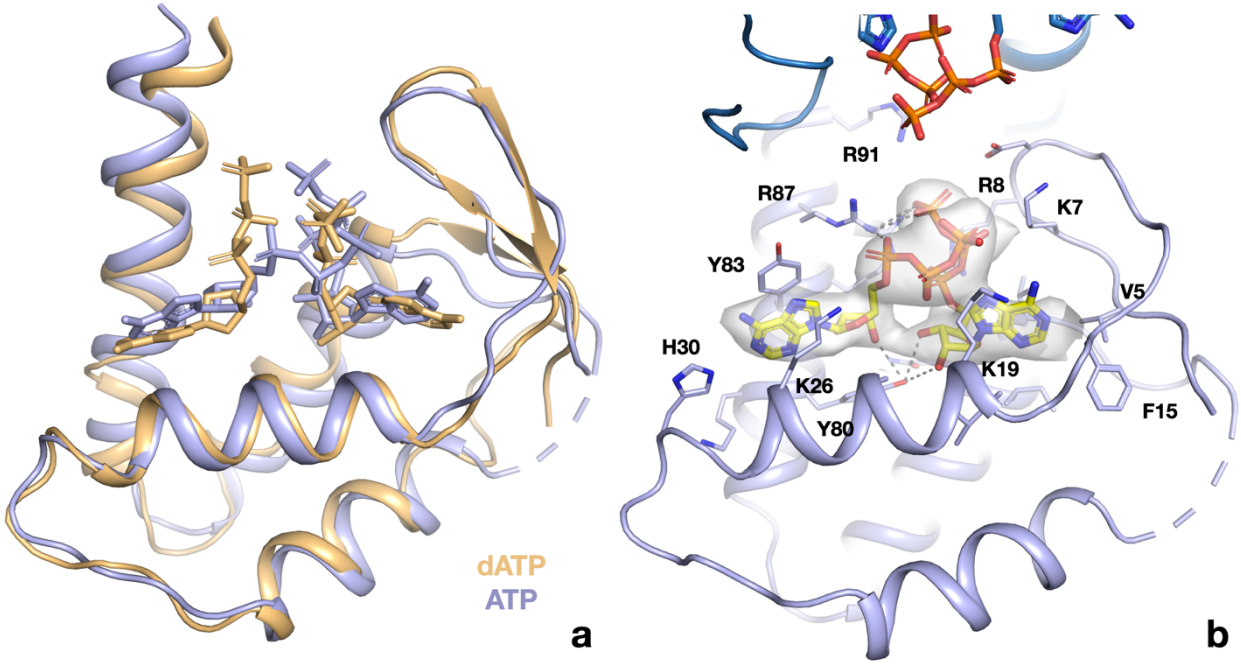

Figure 9 – figure supplement 2. ATP and dATP bind differently to the PcNrdD ATP-cone. a) Comparison of the overall binding modes. The dATP complex is in beige, the ATP-CTP complex in light blue. Nucleotides are shown as sticks. Missing loops are shown as dotted lines. B) Details of the interactions of ATP with the ATP-cone in the ATP-CTP complex (compare to Figure 9e). The second ATP-cone of the pair at the top of the panel is drawn in a darker shade of blue and the phosphate groups of the ATP molecules bound to it are visible.

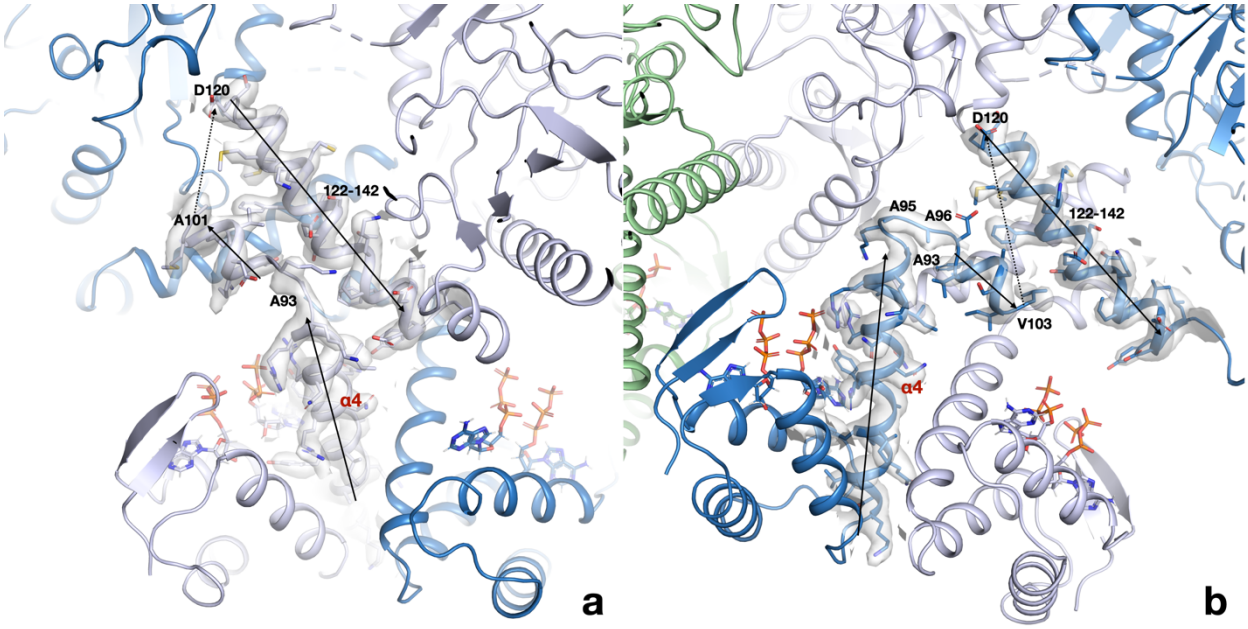

Figure 9 – figure supplement 3. The linker region between the ATP-cone and the first helix of the core domain interacts very differently in the two monomers of each dimer. Panel A shows the conformation in chains A and C, panel B shows chain B and D. The region around residues 93-97 adopts two very different conformations and as a consequence the following short helix is either parallel to the first helix of the core domain in chains A/C or antiparallel in chain B/D. Chain A is drawn in light blue, chain B in dark blue. The cryo-EM map is shown as a transparent surface.

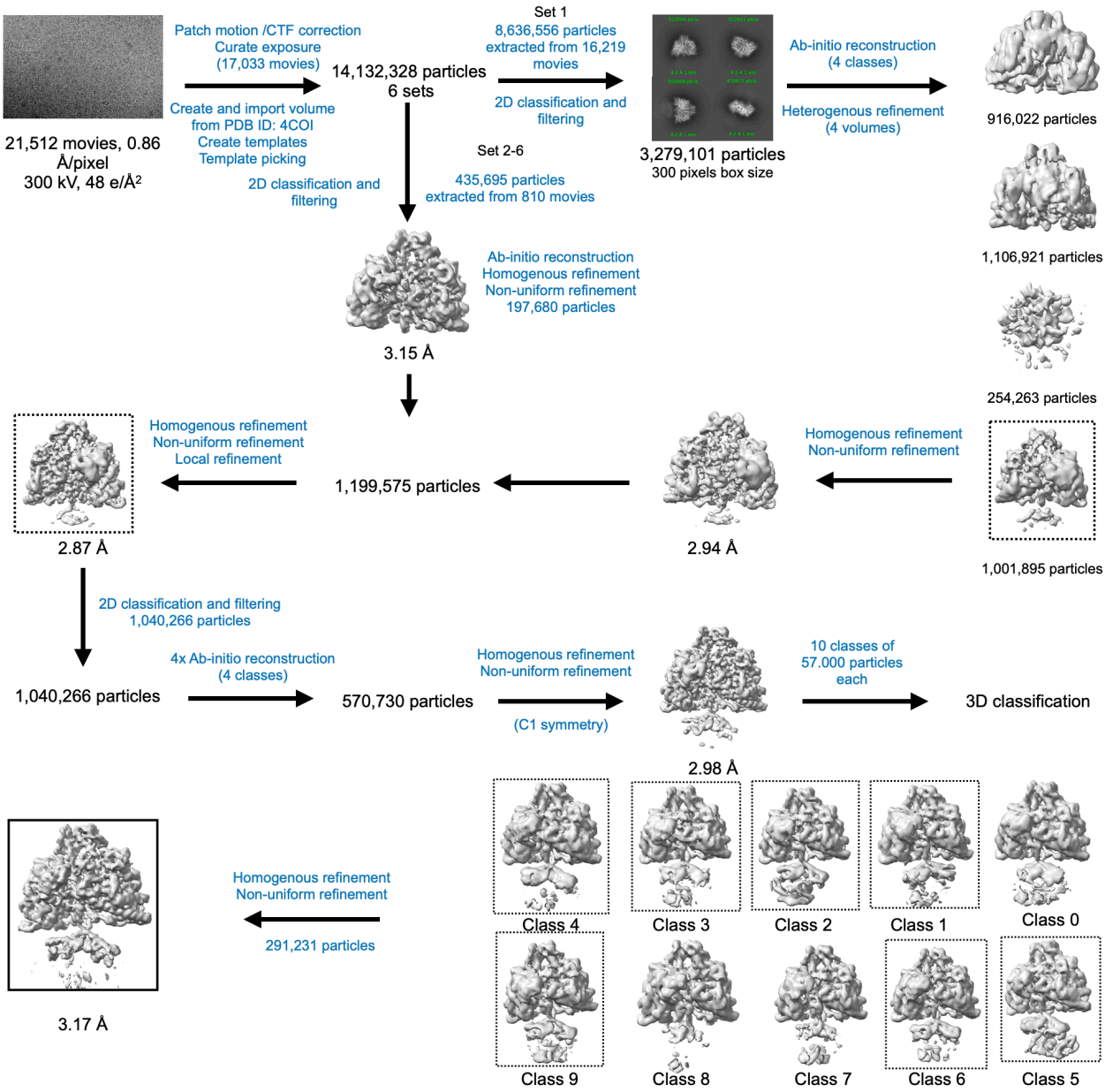

Table 1 - table supplement 1. Cryo-EM data processing workflow for PcNrdD in the presence of ATP-CTP.

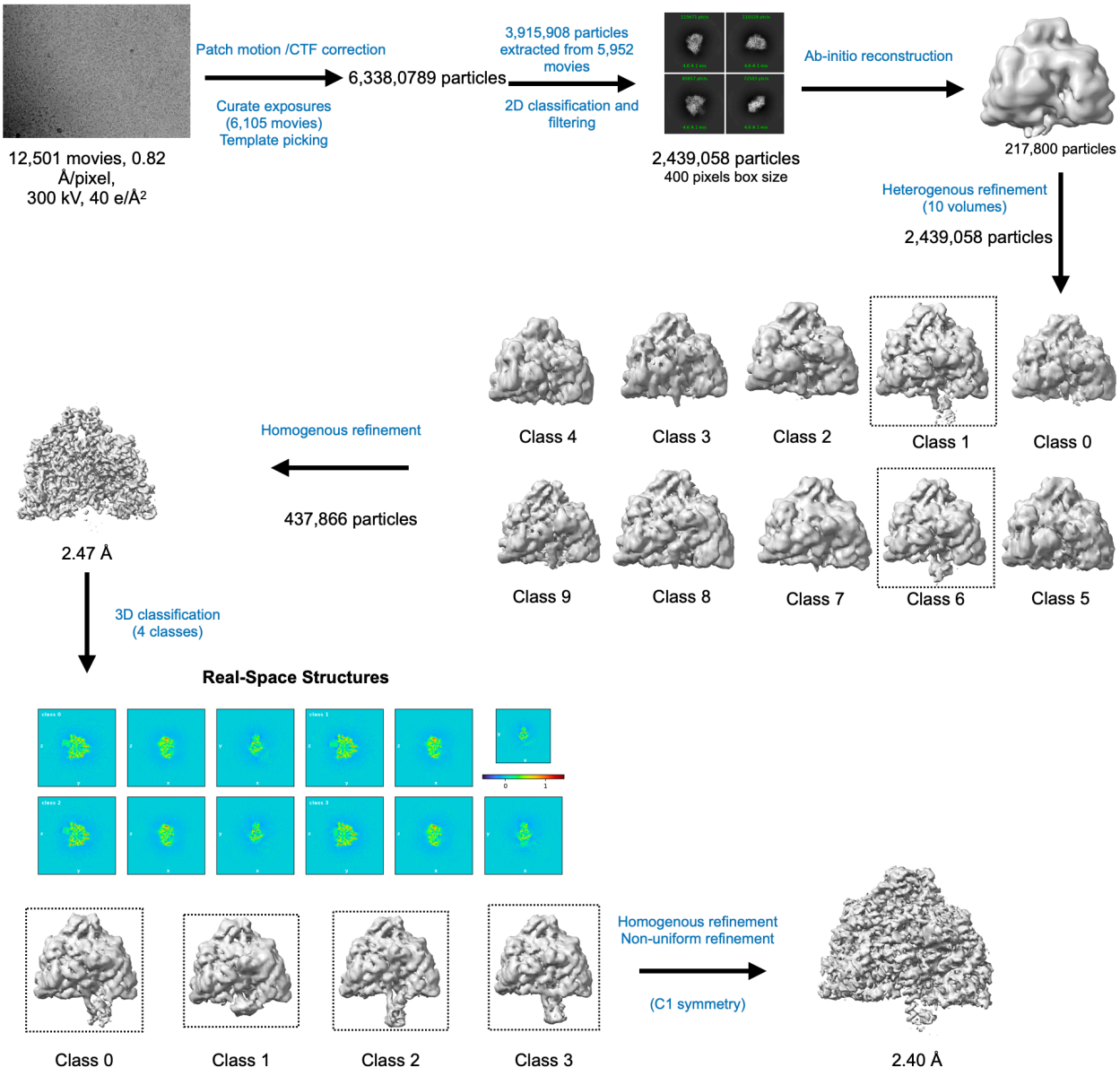

Table 1 - table supplement 2. Cryo-EM data processing workflow for PcNrdD in the presence of ATP-dTTP-GTP.

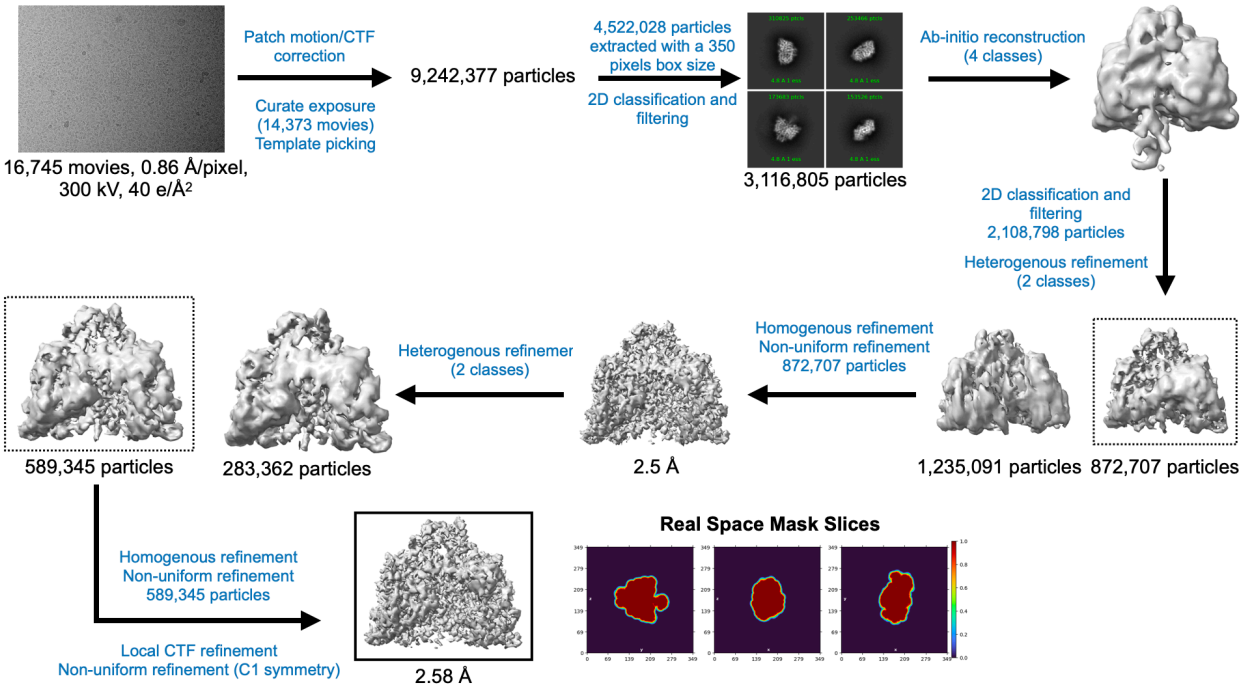

Table 1 - table supplement 3. Cryo-EM data processing workflow for PcNrdD in the presence of ATP-dGTP.

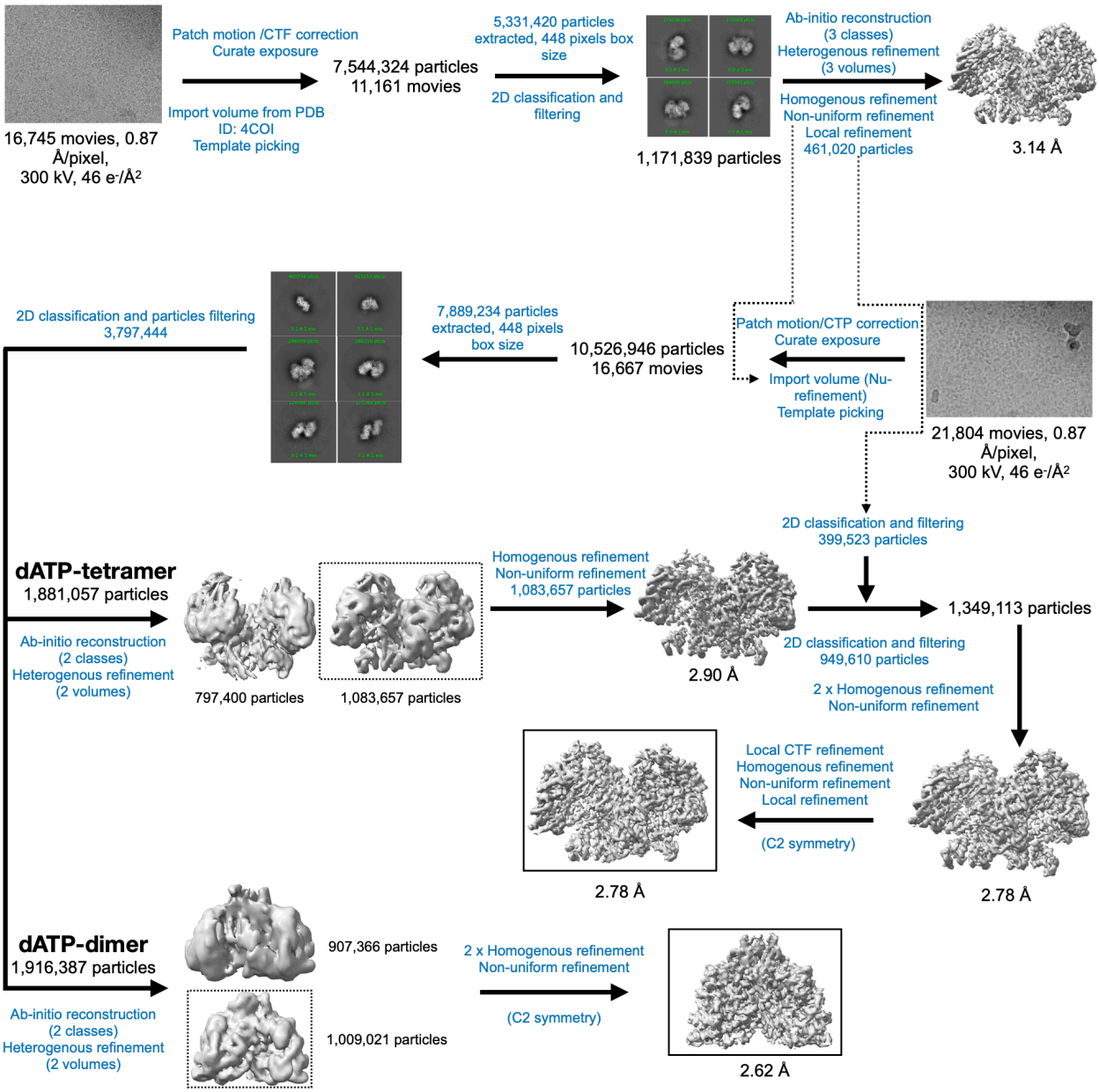

Table 1 - table supplement 4. Cryo-EM data processing workflow for PcNrdD in the presence of dATP.

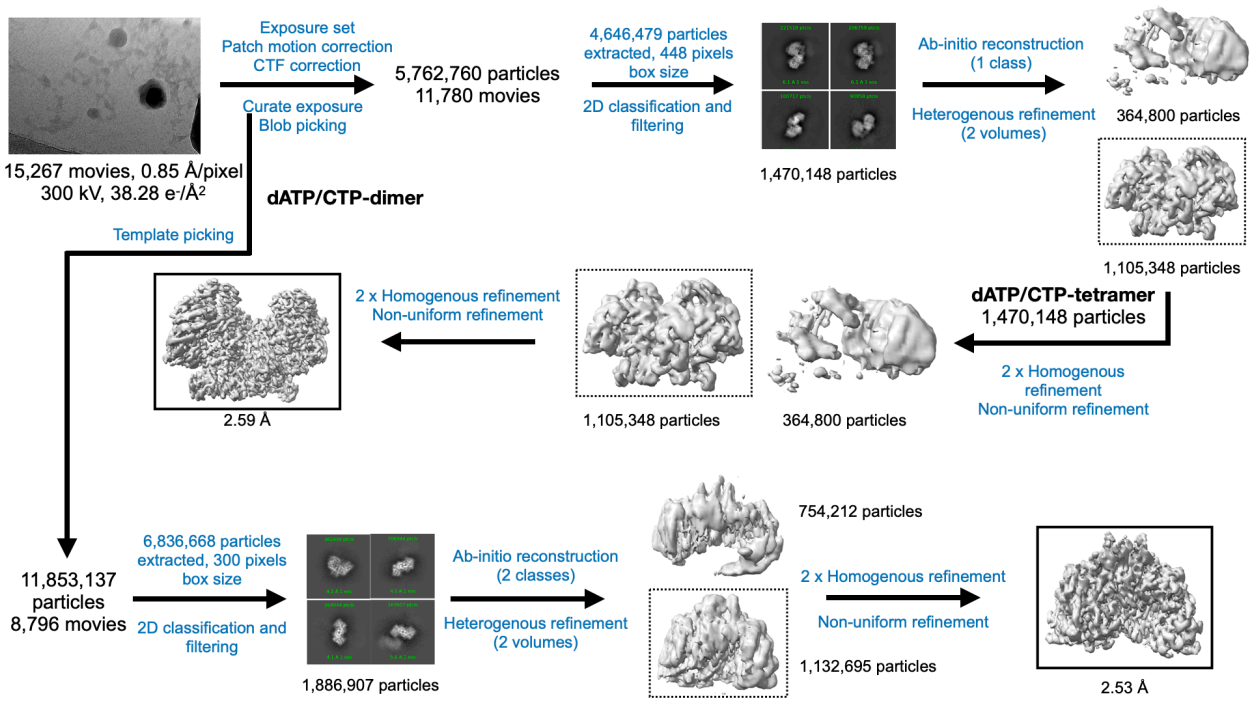

Table 1 - table supplement 5. Cryo-EM data processing workflow for PcNrdD in the presence of dATP/CTP.